Biophysical *Journal*
Article

Biophysical Society

Highly Disordered Amyloid-β Monomer Probed by Single-Molecule FRET and MD Simulation

Fanjie Meng,[1] Mathias M. J. Bellaiche,[1,2] Jae-Yeol Kim,[1] Gül H. Zerze,[3] Robert B. Best,[1,*] and Hoi Sung Chung[1,*]
[1]Laboratory of Chemical Physics, National Institute of Diabetes and Digestive and Kidney Diseases, National Institutes of Health, Bethesda, Maryland; [2]Department of Chemistry, University of Cambridge, Cambridge, United Kingdom; and [3]Department of Chemical and Biomolecular Engineering, Lehigh University, Bethlehem, Pennsylvania

ABSTRACT Monomers of amyloid-β (Aβ) protein are known to be disordered, but there is considerable controversy over the existence of residual or transient conformations that can potentially promote oligomerization and fibril formation. We employed single-molecule Förster resonance energy transfer (FRET) spectroscopy with site-specific dye labeling using an unnatural amino acid and molecular dynamics simulations to investigate conformations and dynamics of Aβ isoforms with 40 (Aβ40) and 42 residues (Aβ42). The FRET efficiency distributions of both proteins measured in phosphate-buffered saline at room temperature show a single peak with very similar FRET efficiencies, indicating there is apparently only one state. 2D FRET efficiency-donor lifetime analysis reveals, however, that there is a broad distribution of rapidly interconverting conformations. Using nanosecond fluorescence correlation spectroscopy, we measured the timescale of the fluctuations between these conformations to be ∼35 ns, similar to that of disordered proteins. These results suggest that both Aβ40 and Aβ42 populate an ensemble of rapidly reconfiguring unfolded states, with no long-lived conformational state distinguishable from that of the disordered ensemble. To gain molecular-level insights into these observations, we performed molecular dynamics simulations with a force field optimized to describe disordered proteins. We find, as in experiments, that both peptides populate configurations consistent with random polymer chains, with the vast majority of conformations lacking significant secondary structure, giving rise to very similar ensemble-averaged FRET efficiencies.

INTRODUCTION

Amyloid-β (Aβ) protein is a fragment comprising between 39 and 43 residues of amyloid precursor protein found in amyloid plaques in the brains of Alzheimer's disease patients (1). X-ray fiber diffraction and solid-state NMR have shown that the Aβ fibrils found in these plaques contain ordered cross-β structures (2–4). There is considerable complexity, however, at the molecular scale: solid-state NMR structures of fibrils formed by the 40-residue (Aβ40) (5–7) and 42-residue (Aβ42) proteins (8–10) are quite different and structural polymorphism is found even in the fibrils of the same protein isoform depending on aggregation conditions (11–13). In addition, recent studies have shown that the structure of fibrils seeded from material derived from patients is different from those grown in vitro from the monomer state (7,14). Beyond this structural heterogeneity, the mechanism of fibril formation is also nontrivial and the hardest to study experimentally due to the heterogeneity and transient nature of the initial oligomers. Aggregation of Aβ is characterized by a rapid fibril growth phase preceded by a long lag period, which is required for the formation of aggregation seeds (15). Once an aggregation seed is formed, it acts as a template for fibril elongation. The fibrils themselves can also accelerate the formation of seeds for new fibrils, a process known as "secondary nucleation" (16). Although the same overall kinetic mechanism appears to describe both proteins, aggregation of Aβ42 is much faster than that of Aβ40 (17) and the relative importance of primary versus secondary nucleation differs (18,19). In addition to seeding aggregation, recent studies have suggested that oligomers may be more toxic than fibrils and interact with various cellular components and synaptic receptors (20–23). Therefore, characterization of the seed formation from monomers should be helpful for understanding the complexity and heterogeneity of the process and possibly the disease mechanism.

As a first step to understanding the assembly, monomers of Aβ have been extensively studied, mostly using solution

---

Submitted September 5, 2017, and accepted for publication December 18, 2017.

*Correspondence: chunghoi@niddk.nih.gov or robert.best2@nih.gov

Fanjie Meng and Mathias M. J. Bellaiche contributed equally to this work.

Editor: Elizabeth Rhoades.

https://doi.org/10.1016/j.bpj.2017.12.025

NMR and molecular dynamics (MD) simulations. A consensus of conclusions of these studies is that Aβ is largely disordered and does not have a large fraction of stable conformations. Nonetheless, many studies have suggested that local secondary structures or transient conformations with tertiary contacts exist, although the structures and populations of these conformations vary among studies (24–28) despite similarities in experimental conditions (neutral pH and 4–8°C). Because the only difference between Aβ40 and Aβ42 is the two additional hydrophobic residues at the C-terminus of Aβ42, the interpretation of different behaviors of the two peptides has been focused on the effect of these two residues. For example, Yan et al. (26) have used NMR relaxation data to suggest that the C-terminal end of Aβ42 is more rigid and shows a higher β-strand propensity than that of Aβ40, which may have implications in explaining the increased aggregation rates of Aβ42. In a study of the decapeptide Aβ21–30 identified by limited proteolysis, Lazo et al. (29) raised a possibility of the formation of a β-turn in the hydrophilic region (residue 23–30) that resembles the solid-state NMR structure of Aβ40 fibril (30); long-range contacts required for this hairpin structure were not, however, observed in the MD simulation and NMR study by Fawzi et al. (31) for the same peptide. In the most recent and extensive NMR study, at 4°C, Roche et al. (32) have shown that the chemical shifts and *J* couplings of both Aβ40 and Aβ42 minimally deviate from those of a random coil, and, more strikingly, there is virtually no difference in these values between the two proteins from the N-terminus to residue 34. In addition, there are no long-range nuclear Overhauser effects (NOEs) in either protein, contrary to earlier studies (28,33,34). This result strongly suggests that both Aβ40 and Aβ42 are predominantly disordered, very similar to each other, and that the population of compact structures, such as β-hairpins, in the hydrophilic region is very low or negligible.

MD simulations are a valuable addition to experiment for characterizing disordered proteins, as determining structural features of a heterogeneous distribution of conformations from ensemble-averaged experimental data is clearly very challenging. The results of past simulation studies, however, vary largely in various measures such as the secondary structure content and the nature of representative conformations. Garcia and co-workers (35–38) have observed a more structured C-terminus for Aβ42 than for Aβ40, a strong propensity for turn formation in the hydrophilic region (residues 24–28), and relatively high secondary structure contents. In contrast, Lin and co-workers (39,40) have reported significantly reduced β-contents in this region. Head-Gordon and co-workers (33,34) have performed a number of studies of Aβ40 and Aβ42 as well as derived fragments, with careful comparison to NMR data. They found that a broad ensemble of local secondary structure was formed in both Aβ40 and Aβ42. They also suggested significant differences in where local β-structure was formed in the two peptides. One likely reason for the discrepancies between the various studies is residual inaccuracies of the force fields, to which disordered proteins are particularly sensitive, as well as the challenge of adequately sampling the disordered ensemble. The first of these systematic errors is the relative propensity for forming different types of secondary structure, a deficiency that has largely been corrected in newer force fields by empirical corrections using solution NMR data (41). In addition, until recently, unfolded proteins were more compact than observed experimentally; in the past 2 years, this has also been addressed by modifying the simulation water models (42–46). Somewhat remarkably, given this difficulty, the simulation results have always been found to be consistent with experimental observations, usually solution NMR data such as chemical shifts, *J*-couplings, and short-range NOEs (33–36). Part of the explanation for this may be that those parameters are primarily sensitive to local structure in a disordered chain. Complementary information on the global chain dimensions should better help to discriminate between different models. In principle, one source of such information could be NMR data obtained from paramagnetic relaxation enhancement and residual dipolar couplings (47,48).

In this work, we compare the behaviors of Aβ40 and Aβ42 using a close combination of single-molecule Förster resonance energy transfer (FRET) spectroscopy and MD simulations. Single-molecule spectroscopy can virtually eliminate one of the key difficulties in quantitative experimental characterizations of the monomeric state of Aβ: namely the formation of oligomers and larger aggregates at high micromolar concentrations. This is because the experimental concentration is so low (100 pM or below) and the detection of a monomer can be ensured by observation of a single photobleaching step of the dyes. This avoids the need to perform experiments at low temperatures to slow down the aggregation, as often done in NMR studies. A second advantage of FRET is that it probes global, long-range intramolecular distances, thus complementing the more local information provided by many NMR observables. We labeled the N- and C-termini of Aβ with Alexa 488 and Alexa 647 site-specifically by incorporating an unnatural amino acid, 4-acetylphenylalanine (49,50) at the N-terminus and cysteine at the C-terminus to exclude any potential ambiguity caused by the two species with different donor and acceptor positions. We compared FRET efficiencies of the two proteins in solution and after immobilization on a glass surface at room temperature. We found that each protein apparently populates a single state, with Aβ42 being slightly more compact than Aβ40. However, 2D FRET efficiency-donor lifetime analysis shows that there is a distribution of different conformations, which are rapidly interconverting, similar to unfolded proteins. We did not observe any dynamics on the timescale longer than ~1 μs except acceptor photoblinking, whereas nanosecond fluorescence correlation spectroscopy (nsFCS) experiments measured an end-to-end distance relaxation time of ~35 ns, which agrees well with those measured for other intrinsically disordered proteins (IDPs) (51,52). Nanosecond-timescale conformational fluctuation has also been observed for an amyloid forming protein, the N-terminal region of the yeast prion protein Sup35 (53). These results suggest that both proteins are disordered and there is no significant population of a stable ordered structure, which is consistent with the most recent NMR result (32). However, the observed FRET efficiency values of both isoforms are much lower than those expected from previous MD simulation studies, which have reported disordered but compact conformational ensembles.

Our MD simulation results give a consistent picture of the peptide structure and dynamics. We ran both conventional and temperature replica-exchange MD (REMD) of both isoforms in explicit solvent using two recently developed force fields that do not suffer from the systematic global drive toward collapse and artificial stabilization of secondary structure in IDPs observed using earlier energy functions (44,54). The simulations are consistent with previously published NMR data, reflecting primarily local structure formation. In addition, we find that both peptides have virtually indistinguishable ensemble-averaged radii of gyration R_g, end-to-end distances R_{ee}, and FRET efficiencies E, as in the single-molecule experiments. Distributions of these parameters, however, show a very small population at low R_{ee} for Aβ42 that is absent for Aβ40. Performing a machine learning cluster analysis of the peptides' contact maps allows us to resolve the conformational ensemble into groups of structures with similar properties. As expected, these analyses show that the vast majority of populated states are random coil. However, we do find a very small subpopulation of states in the ensemble of Aβ42 that differs significantly from other states of Aβ42 and all states of Aβ40 in that it exhibits long-range terminal contacts that result in hairpin formation. This local β-structure is responsible for the low R_{ee} probability shoulder and is consistent with the marginally higher FRET efficiency observed for freely diffusing Aβ42 compared with that of Aβ40.

MATERIALS AND METHODS

Materials

Details of the expression, purification, and dye-labeling of proteins are described in the Supporting Material.

Single-molecule spectroscopy

Details of free-diffusion, immobilization, and nsFCS experiments are described in the Supporting Material. For the accurate determination of the FRET efficiency and donor lifetime, we performed various corrections for background, donor leak into the acceptor channel, ratios of the detection efficiencies, and quantum yields of the donor and acceptor (γ-factor) and acceptor blinking (55,56). See the Supporting Material for the details.

MD simulation

Details of the REMD simulations are described in the Supporting Material. Briefly, we ran long isobaric-isothermal simulations on the order of 750 ns for each peptide using a temperature ladder from $T = 277$ K to $T = 355$ K in steps of 2 K, using both the Amber ff99SBws and Amber ff03ws force fields. Both optimized force fields give consistent results, demonstrating that our observations are not systematic artifacts. We report in the main text the results from Amber ff99SBws at 299 K with 20 mM NaCl, with analogous results for Amber ff03ws at 299 K included in the Supporting Material. The results from both force fields at 277 K are also consistent with experimental NMR signals. In addition, we ran multiple long simulations with chromophores attached to obtain dynamical properties. Further details are given in the Supporting Material.

RESULTS AND DISCUSSION

Single-molecule free-diffusion experiment shows that Aβ is disordered

We performed two types of single-molecule experiments. First, by immobilizing molecules on a polyethylene glycol (PEG)-coated glass surface, it is possible to collect long fluorescence trajectories, which allows for accurate determination of FRET efficiencies and fluorescence lifetimes. However, there is a possibility that protein-surface interactions can affect the observed protein conformations and dynamics even though the surface is coated with PEG. In addition, the linker amino acid sequence required for immobilization may also affect protein conformations and dynamics. Therefore, we employed a second experiment, in which molecules freely diffuse in solution and a burst of fluorescence is detected when a molecule crosses the confocal volume. There is no protein-surface interaction in this experiment as long as the focus is sufficiently far from any surface. However, the residence time in the focal volume is relatively short (~1 ms), which leads to a shot-noise broadening of the FRET efficiency distribution due to the limited photons collected, and limits the measurable timescale of dynamics to a few milliseconds (57). Our experimental strategy was to perform both experiments and compare the mean FRET efficiencies obtained from the two experiments. If these values are similar, this would lend confidence to more detailed analyses of the data obtained from immobilization experiments.

Fig. 1 shows four protein constructs used in the free-diffusion experiment: Aβ40 and Aβ42, with and without an immobilization tag (AviTag) sequence. Details of the gene construction and incorporation of an unnatural amino acid are described in Protein Expression and Incorporation of an Unnatural Amino Acid in the Supporting Material. Alexa 488 (donor) and Alexa 647 (acceptor) were attached to the N- and C-termini site-specifically. Two shorter sequences of Aβ40 and Aβ42 without the immobilization

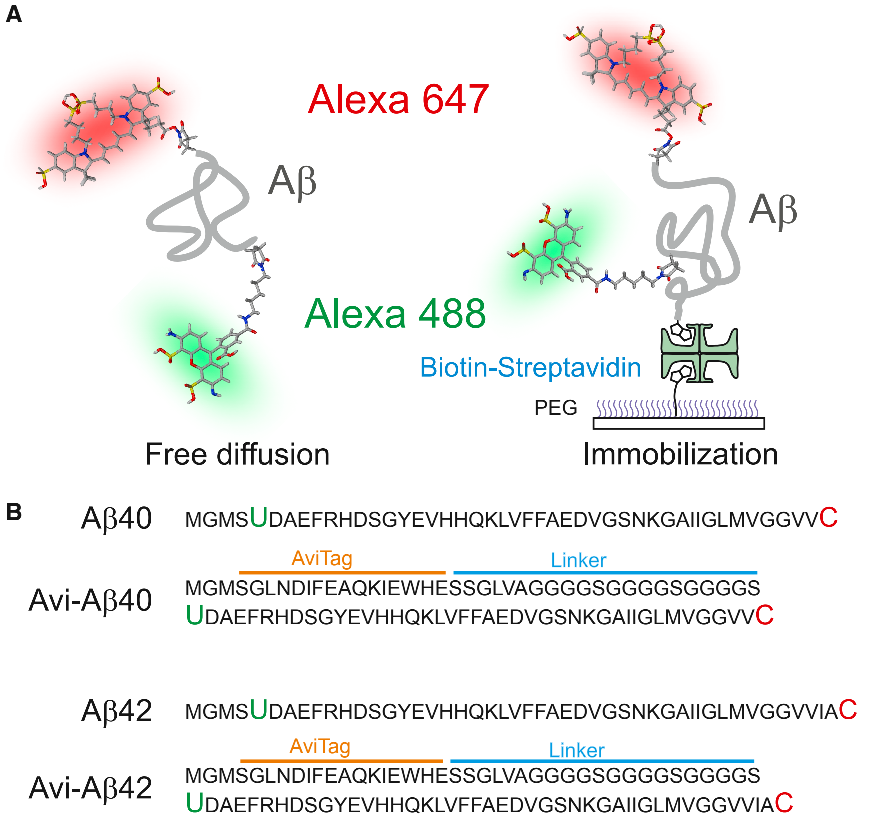

FIGURE 1 Schematic diagram of four amyloid β-protein constructs. (*A*) Aβ40 and Aβ42 (*thick gray lines*) are labeled with Alexa 488 (donor) and Alexa 647 (acceptor) site-specifically at the N- and C-termini, respectively. Experiments were carried out in the free-diffusion mode (*left*) or with molecules immobilized on a PEG-coated glass surface via a biotin-streptavidin linkage (*right*). (*B*) Amino acid sequence of the four proteins. Alexa 488 hydroxylamine is attached to the unnatural amino acid (4-acetylphenylalanine, green U) and Alexa 647 maleimide is attached to the cysteine residue (*red* C). For immobilization, a biotin acceptor sequence (AviTag) is added to the N-terminus of Aβ (Avi-Aβ). The glycine-rich flexible linker is inserted between AviTag and the protein to prevent potential protein-surface interactions. To see this figure in color, go online.

tag were designed as the least perturbed constructs for the free-diffusion experiment. These constructs serve as controls for those with AviTag (Avi-Aβ) to characterize the potential interference of AviTag and the linker in Aβ protein conformations and dynamics.

FRET efficiency histograms ($E = n_A/(n_A + n_D)$, where n_A and n_D are respectively the numbers of detected acceptor and donor photons) of these four constructs are compared in Fig. 2. FRET efficiency distributions measured (40–100 pM protein concentration) in phosphate-buffered saline (PBS) at room temperature (22°C) (*top row* in Fig. 2) show only one peak at $E \sim 0.6$. The other peak near $E = 0$ results from the molecules without an active acceptor (either unlabeled or photobleached). The single peak at $E \sim 0.6$ can be explained by the protein having a single state on the millisecond timescale (the bin time is 2 ms). This state could be a disordered (unfolded) state as the FRET efficiency is similar to that of a 42-residue IDP, the tetramerization domain of p53 (56). It is also possible, however, that this state could be well structured. To rule out this second possibility, we investigated the denaturant dependence of the FRET efficiency distributions. As the urea concentration is increased, the single peak gradually moves to the lower FRET efficiency side (Fig. 2, *A* and *B*). This result strongly suggests that the proteins are already unfolded under native conditions (PBS). The gradual decrease in the FRET efficiency is consistent with gradual expansion of polypeptide chains observed in proteins unfolded by chemical denaturant and IDPs (53,58–66). Even for two-state proteins for which separate folded and unfolded peaks are expected, however, it is possible to observe a single peak whose FRET efficiency shifts with denaturant concentration. This occurs when the exchange between the folded and unfolded states is much faster than the bin time (2 ms), as seen in fast-folding proteins such as the 35-residue subdomain of villin headpiece and WW domain (67–69). This possibility will be discussed in the immobilization experiment section below.

Another notable feature is that the FRET efficiency of Avi-Aβ is slightly lower than that of Aβ without the immobilization tag for both Aβ40 and Aβ42 (Fig. 2 *D*). This difference may result from the slightly higher net negative charge of Avi-Aβ compared to that without a tag (−7 vs. −3), which may increase electrostatic repulsion, or from the excluded volume effect of the additional amino acid sequence at the N-terminus of Avi-Aβ, which prohibits certain conformations with two dyes close to each other. The increase of the FRET efficiency (collapse of unfolded molecules) by the addition of 1 M NaCl supports the former (Fig. 2, *C* and *D*). In any case, the similar FRET efficiency values indicate that the effect of the immobilization tag on the conformational dynamics of Aβ is small.

Although the FRET efficiencies of Aβ40 and Aβ42 in PBS are very similar, the FRET efficiency of Aβ42 is slightly higher than that of Aβ40, despite the two extra

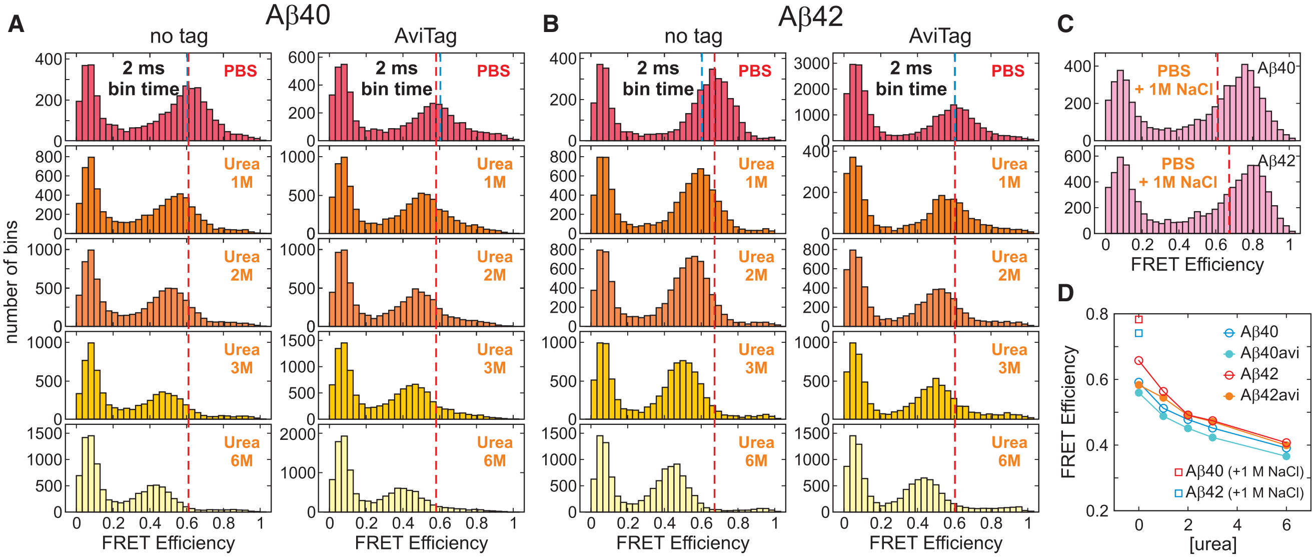

FIGURE 2 FRET efficiency histograms obtained from free diffusion experiments for Aβ40 (*A*) and Aβ42 (*B*). (*A* and *B*) Apparent (uncorrected) FRET efficiencies were calculated using the photons collected in 2 ms bins ($\geq$30 photons). "No tag" stands for the protein samples without AviTag and linker and AviTag represents Avi-Aβ. Blue dashed lines indicate the center of the FRET efficiency peak (Gaussian fit) of Avi-Aβ42 measured in PBS and are drawn for the comparison of the FRET efficiencies between different constructs. Red dashed lines indicate the center of the peaks of individual constructs measured in PBS. The FRET efficiency decreases gradually as the urea concentration is increased, indicating the expansion of disordered proteins. (*C*) Apparent FRET efficiency histograms for Aβ40 (*top*) and Aβ42 (*bottom*) without AviTag in PBS with the addition of 1 M NaCl. Red dashed lines indicate the center of the peaks of the histograms measured in PBS. (*D*) FRET efficiency changes as a function of urea concentration. FRET efficiencies were corrected for background, donor leak, and γ-factor. Square symbols are the data collected in PBS with an additional 1 M NaCl. To see this figure in color, go online.

residues. This small difference is not an artifact, because the result is consistent in the three different cases: Aβ without AviTag and Avi-Aβ in free-diffusion experiments, and the immobilization experiment in the next section (see Table S1 for the comparison). The higher FRET efficiency of Aβ42 may result from greater hydrophobic collapse induced by two additional C-terminal residues, or from differences in local structure. We have performed molecular simulations to address this issue, as discussed below.

Immobilized Aβ shows no conformational transitions on the μs to ms timescale

To collect single-molecule trajectories, long enough to measure the submillisecond dynamics, we immobilized Aβ molecules on a glass surface and acquired >600 trajectories for both Aβ40 and Aβ42 in PBS. The representative fluorescence and FRET efficiency trajectories obtained by continuous-wave excitation are shown in Fig. 3 *A*. Most of the trajectories show a constant FRET efficiency level near $E = 0.6$ for both Aβ40 and Aβ42 without any transition before photobleaching of the donor or acceptor. The FRET efficiency histograms constructed from the mean values of 1-ms bins show a single peak (*lower panels* in Fig. 3 *B*) similar to the free-diffusion data in Fig. 2. The mean FRET efficiencies are similar to those in the free-diffusion data, and the FRET efficiency of Aβ42 is slightly higher than that of Aβ40, consistent with the free-diffusion data in Fig. 2. The width of the peak in the immobilization data is narrower than that of the free-diffusion data because of higher photon count rates (50–100 ms^{-1}) and consequently smaller shot noise. The similarity of the results in the two types of experiments suggests that the effect of immobilization is very small.

As mentioned above, even though there is only one peak in the FRET efficiency distribution, it is possible that there are multiple states that interconvert much more rapidly than the bin time of 1 ms. In fact, numerous simulation and NMR studies have raised the possibility that stable conformations such as a turn in the hydrophilic region (residue 22–30) (27,29,36) could exist transiently. This structure has been of particular interest because it resembles the structure of the fibril of Aβ40 (30), which suggests this transient structure can be a template for fibril formation. Lazo et al. (29) found that this region was resistant to enzymatic cleavage and the stability of the 10-residue peptide (residue 21–30) was correlated with the aggregation propensity of the mutant Aβ proteins (70). Yamaguchi et al. (27) observed that the NMR signal of monomer Aβ became weaker and eventually disappeared as the temperature was raised, which was attributed to the fast chemical exchange between unstructured and a hairpin structure in the hydrophilic region. If this structure exists, we anticipate that its FRET efficiency is higher than 0.6 because the average end-to-end distance will be shorter. In fact, there is a small fraction of molecules exhibiting high FRET efficiencies ($E = 0.7$–0.8) in Fig. 3 *B* (*upper panels*) and Fig. 4 *B*. However, >50% of these molecules show slow and irreversible FRET efficiency changes,

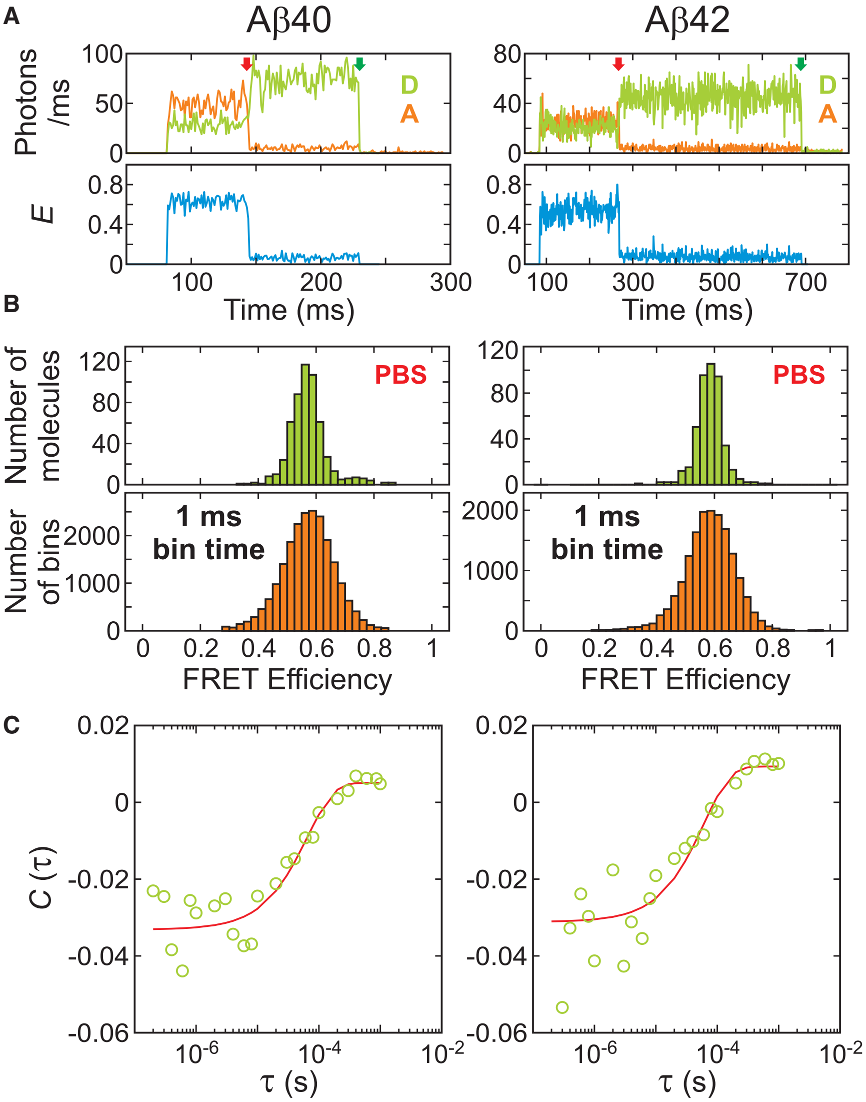

FIGURE 3 Immobilization experiment to probe the conformational dynamics of Aβ40 (*left*) and Aβ42 (*right*) on the timescale of microseconds to milliseconds. Experiments were performed at the native condition (PBS, 22°C). (*A*) Representative fluorescence (D, donor; A, acceptor) and FRET efficiency (*E*) trajectories of Aβ40 and Aβ42 (1 ms bin time) obtained by continuous-wave excitation. Photon count rates were 50–100 ms^{-1}. Both trajectories show a constant FRET efficiency ($E = 0.5$–0.6) followed by successive acceptor (*red arrow*) and donor (*green arrow*) photobleaching. (*B*) The FRET efficiency histograms in the upper panels are constructed using the FRET efficiency values calculated from the initial segment of the trajectory of each molecule. The histograms in the lower panels are constructed using the FRET efficiency values of all 1 ms bins in the initial segment of each trajectory. FRET efficiencies were corrected for background photons. (*C*) Donor-acceptor cross correlation averaged over the initial segments of trajectories in (*B*). Experimental data (*green circles*) are fitted to a single exponential function (*red*). The relaxation rates are 15.3 and 16.5 ms^{-1} for Aβ40 and Aβ42, respectively. To see this figure in color, go online.

which we attribute to the unusual photophysics of Alexa 647 (56) (see Fig. S1, A and B).

To probe any fast dynamics, we first calculated the average donor-acceptor cross-correlation function (see Eq. S17 in the Supporting Material) of the segments containing both donor and acceptor fluorescence of the immobilized trajectories (Fig. 3 *C*). There are low-amplitude decays for both proteins, and single-exponential fitting yields relaxation times of 65 and 61 μs for Aβ40 and for Aβ42, respectively (see Table S2). One explanation for this relaxation could be conformational exchange such as the hairpin formation dynamics mentioned above (27).

To obtain more detailed information, we used a maximum likelihood method that analyzes photon trajectories directly without binning and extracts FRET efficiencies, relative populations of states, and rate coefficients between them (69,71). We first used the simplest two-state model (see Maximum Likelihood Analysis of Acceptor Blinking in the Supporting Material). The extracted apparent (uncorrected) FRET efficiencies of the two states are 0.60 (0.61) and 0.13 (0.13), the population of the high-FRET state is 0.93 (0.94), and the relaxation rate is 12.2 ms^{-1} (14.1 ms^{-1}) for Aβ40 (Aβ42) (Table S2). These relaxation rates are similar to those obtained from the correlation analysis, indicating that the two-state model is a reasonably good model. Because the major species with the high-*E* value ($E \sim 0.6$, 94%) is the disordered state, the low-FRET state should be a potentially structured state if it exists. However, the FRET efficiencies of the low-FRET states, corrected for background, donor-leak (0.05), and γ-factor (ratio of the detection efficiencies and quantum yields of the donor and acceptor) are 0.07 and 0.08 for Aβ40 and Aβ42, respectively. $E = 0.07$ correspond to 8 nm in distance between the two fluorophores (with Förster radius of 5.2 nm), and it is very unlikely that both Aβ40 and Aβ42, which are very short proteins, take this extended conformation with similar stability (lifetime

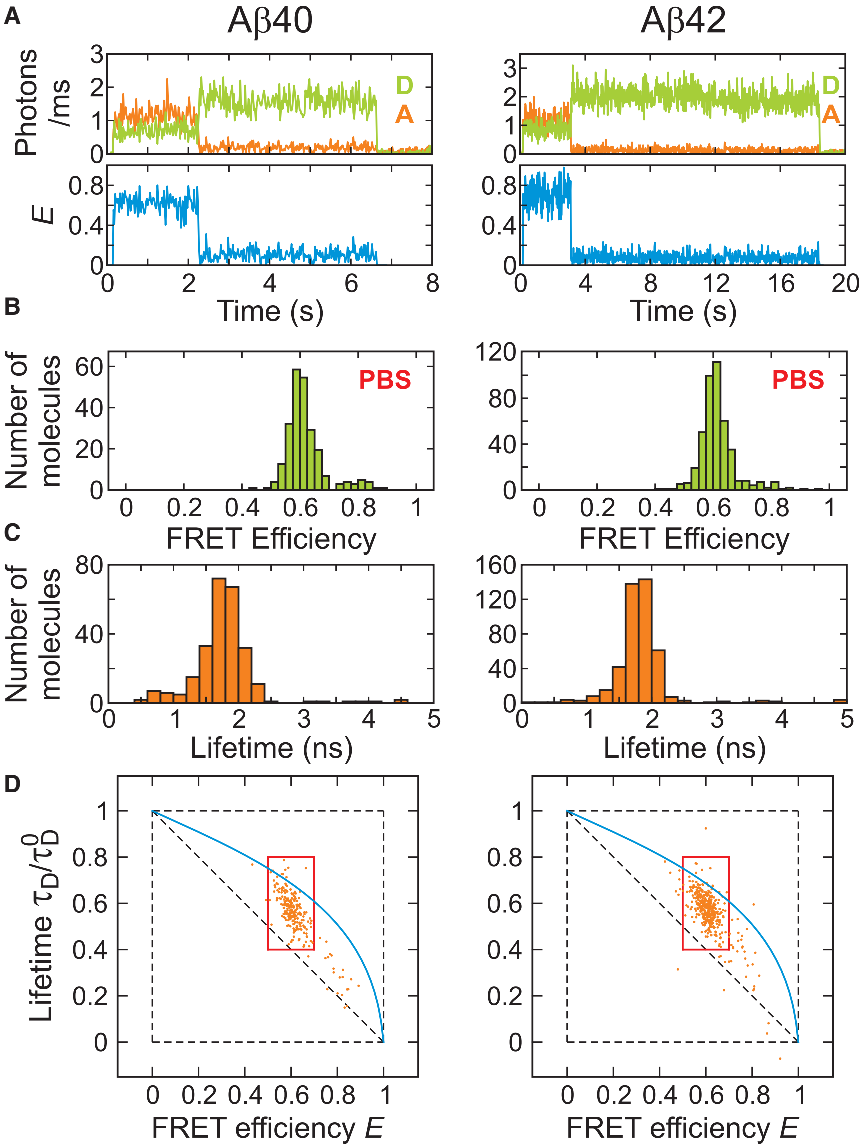

FIGURE 4 FRET efficiency and donor lifetime analysis of immobilized Aβ. (*A*) Representative fluorescence and FRET efficiency trajectories of Aβ40 (*left*) and Aβ42 (*right*) obtained by pulsed-mode laser excitation with 20 MHz repetition rate. The illumination intensity is lowered by 10 times compared to that in Fig. 3 to collect longer trajectories for the accurate determination of donor lifetimes. The bin time is 20 ms. The experiments were performed in PBS (22°C). (*B* and *C*) FRET efficiency and donor lifetime histograms were constructed using the values calculated from the initial segment of each trajectory. Segments containing >1000 photons were analyzed. The FRET efficiency was corrected for background, donor leak into the acceptor channel, γ-factor, direct acceptor excitation, and acceptor blinking. The donor lifetime was corrected for background and acceptor blinking. (*D*) 2D FRET efficiency-donor lifetime plots constructed using the values in (*B*) and (*C*). The shift of the distribution above the diagonal indicates rapid conformational fluctuations of disordered Aβ. The data inside the red rectangles were used to calculate the variance (σ_c^2) of the FRET efficiency distribution caused by these fluctuations. $\sigma_c^2 = 0.07$ ($\pm$0.02) for both Aβ40 and Aβ42. Errors are standard deviations calculated by error propagation using the standard deviation and covariance values of the FRET efficiencies and donor lifetimes in the 2D distributions. The blue solid curve indicates the lifetime dependence on the FRET efficiency of a Gaussian chain. To see this figure in color, go online.

of $\sim$60 μs) and similar relative populations (see Simulation Results in the Supporting Material). Instead, we suspect that this additional state results from acceptor blinking. When the acceptor is in the dark state, there is no energy transfer from the donor, and acceptor intensity decreases whereas donor intensity increases. This appears as anticorrelation in the cross-correlation function. The apparent FRET efficiency of 0.13 is slightly higher than the expected FRET efficiency of the acceptor dark state, which is the same as that of the donor-only (acceptor-bleached) state, 0.06. However, the maximum likelihood analysis with the fixed FRET efficiency of 0.06 for the second state results in similar parameters, including the relaxation rates and relative populations (see Table S2).

The results so far show that both Aβ40 and Aβ42 are disordered, exhibit apparently one state, and there are no conformational dynamics on a timescale longer than $\sim$1 μs. If there is an additional stable state, its population should be much lower than the population of the acceptor dark state, $\sim$5%, or its FRET efficiency should be so similar to that of the disordered Aβ, 0.6, that these are indistinguishable.

2D FRET efficiency-lifetime analysis and nsFCS reveal nanosecond dynamics of disordered Aβ

2D FRET efficiency-lifetime analysis (51,56,61,72–75), which visualizes the correlation between the FRET efficiency and the donor fluorescence lifetime, provides further evidence that Aβ is disordered. For this analysis, we collected trajectories of immobilized molecules illuminated by a picosecond-pulsed laser. In this experiment, in addition to the photon count rates (intensity) of the donor and acceptor, the delay times between the laser pulse and photon arrivals are measured. Representative trajectories and the histograms of the mean FRET efficiency and donor lifetime values calculated for individual trajectories (i.e., individual molecules) are shown in Fig. 4, *A*–C.

The 2D FRET efficiency-lifetime plots in Fig. 4 *D* were constructed using these values. When the distance between the donor and acceptor is fixed (i.e., a single conformation), the FRET efficiency and donor lifetime are related as $\tau_D/\tau_D{}^0 = 1 - E$, where τ_D and $\tau_D{}^0$ are the donor lifetimes in the presence and absence of the acceptor, respectively. In this case, the distribution should be located on the diagonal of the 2D plot. On the other hand, when there is a distribution of conformations with different donor-acceptor distances, which are so rapidly interconverting that the FRET efficiency histogram shows a single peak, the relationship between the FRET efficiency and donor lifetime is different, and given by $\tau_D/\tau_D{}^0 = 1 - E + \sigma_c{}^2/(1 - E)$. The value $\sigma_c{}^2$ is the variance of the FRET efficiency of the underlying conformational distribution (74). (Note that this is not the variance of the peak of the FRET efficiency histograms in Fig. 4 *B*.) In this case, the 2D distribution is positively shifted from the diagonal. This shift results from the fact that the donor lifetime is determined by the donor photons and more donor photons are emitted from the conformations with low FRET efficiency values. In other words, the donor lifetime is the average lifetime weighted by 1 – *E* of the conformations. This shift has been observed in unfolded proteins and IDPs (51,52,56,61,75). As shown in Fig. 4 *D*, both Aβ40 and Aβ42 exhibit a positive shift. This shift can be compared with that of a random polymer model (Gaussian chain), which has been widely used to describe the dynamics of chemically unfolded proteins and intrinsically disordered proteins (51,58,59,61,63,76). In this model, the distance distribution can be obtained from the mean experimental FRET efficiency, and therefore, $\sigma_c{}^2$ can be calculated. The expected donor lifetime is calculated as a function of *E* in Fig. 4 *D*. The $\sigma_c{}^2$ values are 0.07 (±0.02) for both proteins, indicating that they are largely disordered although the values are slightly smaller than 0.11 expected from a Gaussian chain.

As mentioned above, we have not detected any conformational dynamics on a timescale longer than ~1 μs. Therefore, the conformational fluctuations of disordered Aβ should occur on the nanosecond timescale. To determine this timescale, we performed nsFCS experiments (77,78). Fig. 5 shows the correlation functions. All three correlation functions (donor and acceptor autocorrelations and donor-acceptor cross correlation) have three components: antibunching, conformational dynamics, and triplet blinking. The three correlations were fitted to a triexponential function (see Eq. S16 in the Supporting Material), which results in the timescale of the conformational dynamics of 30 and 37 ns for Aβ40 and Aβ42, respectively, similar to those of other IDPs (51–53). The $\sigma_c{}^2$ value calculated from the correlation

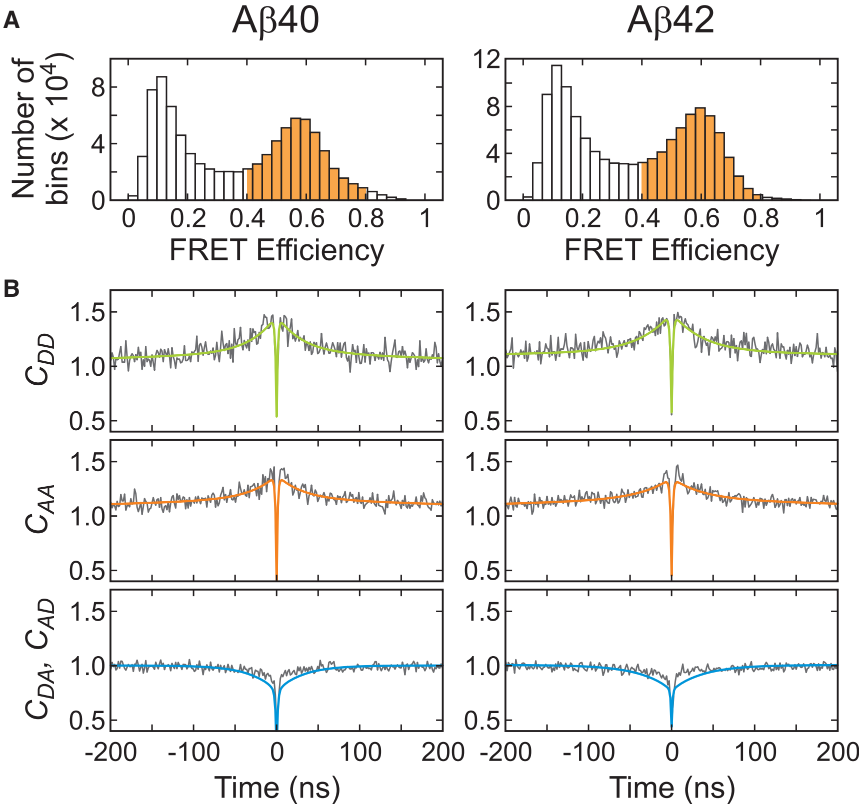

FIGURE 5 nsFCS measurement of Avi-Aβ40 and Avi-Aβ42. (*A*) Fluorescence bursts with FRET efficiencies between 0.4 and 0.8 (shaded in *orange*) were analyzed. (*B*) Global fitting of three correlation data (autocorrelation of the donor and acceptor and cross correlation) results in the conformational fluctuation timescale (τ_{CD}) and $\sigma_c{}^2$ values of 30 (±2) ns and 0.059 (±0.003) for Aβ40 and 37 (±2) ns and 0.057 (±0.002) for Aβ42. $\sigma_c{}^2$ values are consistent with the value 0.07 obtained from the 2D FRET efficiency-lifetime analysis. To see this figure in color, go online.

amplitudes (79,80) (see Eq. S16 in the Supporting Material) and the FRET efficiencies of Avi-Aβ measured in the free-diffusion experiment (Table S1) is 0.06 for both Aβ40 and Aβ42, which agrees very well with the values obtained from the 2D FRET efficiency-lifetime analysis above.

Acharya et al. (81) have recently investigated the chain dynamics of Aβ by monitoring quenching of the triplet state of tryptophan by cysteine. The inferred timescale of the contact formation between residue 4 and residue 35 was several microseconds. The contact formation time is generally much longer than the end-to-end distance correlation time. Although the measured chain diffusion of Aβ42 was ~5 times slower than that of Aβ40, they observed Aβ42 was slightly more compact than Aβ40, similar to our result that the FRET efficiency of Aβ42 is marginally higher than that of Aβ40.

Simulation results

The experimental results above show that both Aβ40 and Aβ42 are largely disordered and their reconfiguration time is ~35 ns. The slightly higher FRET efficiency value of Aβ42 indicates that it is slightly more compact than Aβ40 despite having two more residues at the C-terminus. It is very difficult, however, to investigate the origin of this difference experimentally. To obtain molecular insight into Aβ conformations, we performed all-atom MD simulations in explicit solvent, as described in the Materials and Methods. Most notably, we have used the Amber ff99SBws force field, which has been optimized to reproduce the dimensions of disordered proteins.

We first calculated average configurational quantities for both peptides from REMD simulation. The distributions of radius of gyration (R_g), end-to-end distance (R_{ee}), and E at 299 K, shown in Fig. 6, demonstrate that both peptides populate closely overlapping ensembles for all quantities, with nearly indistinguishable ensemble averages: $\langle R_g \rangle = 1.56 \pm 0.01$ nm (1.59 ± 0.01 nm), $\langle R_{ee} \rangle = 3.80 \pm 0.05$ nm (3.77 ± 0.04 nm), and $\langle E \rangle = 0.68 \pm 0.01$ (0.69 ± 0.01), with a distribution variance of $\sigma_c{}^2 = 0.09$ (0.08) for Aβ40 (Aβ42). Although the FRET efficiency variances agree quantitatively with experimental results, the mean FRET efficiency values are slightly higher than those obtained experimentally. We note, however, that because we are close to the range where efficiency varies most sharply with distance, $\langle E \rangle$ can be altered by relatively small errors in the simulation distance distribution. We illustrate in Fig. S2 the small scaling that would need to be applied to the distance distributions for $\langle E \rangle$ to match experiment. Although the results above were obtained from simulations of unlabeled proteins, we have also performed long equilibrium MD simulations with explicit fluorophores attached, as well as separate REMD simulations with a different force field, with all methods yielding consistent results (Table S1). Although we cannot obtain dynamical properties from the REMD simulations, we have used our long simulations with attached fluorophores to determine the FRET efficiency autocorrelation function. We find an approximately biexponential relaxation for both peptides, with relaxation times of ~4 and ~40 ns (Fig. S3). The faster component would not be visible in the experiment due to overlap with the antibunching contribution to the correlation function, but the slow components are in excellent agreement with the experimental relaxation times. There is the possibility that the difference between the FRET efficiencies derived from simulation and experiment could be due to the

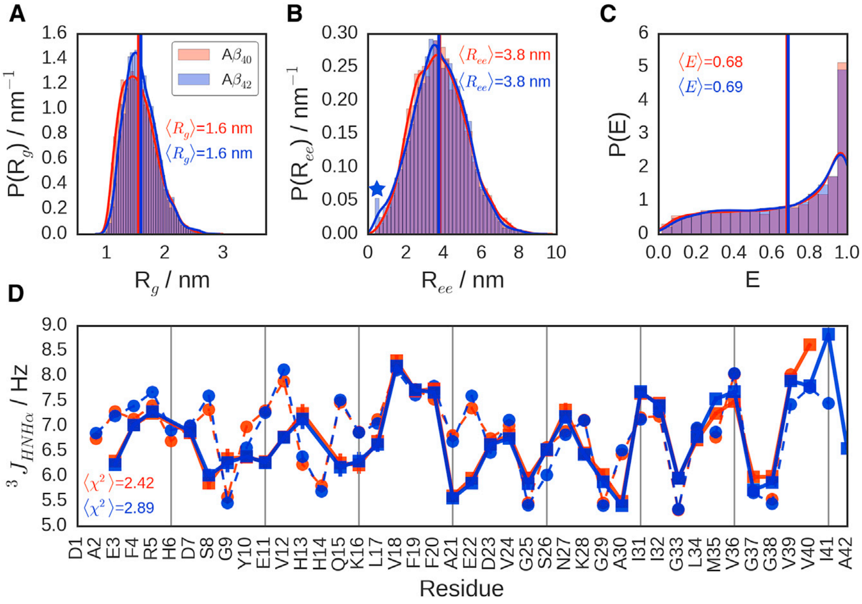

FIGURE 6 Ensemble observables from simulations of Aβ40 (*red*) and Aβ42 (*blue*). (*A–C*) Probability densities for peptide radii of gyration (R_g), end-to-end distances (R_{ee}), and FRET efficiencies (E), showing nearly overlapping distributions and ensemble averages (shown as *vertical lines* and as *text annotations*) for both isoforms. The major difference is the low end-to-end distance probability shoulder observed only for Aβ42, denoted by a blue star in (*B*). (*D*) *J* couplings from simulation (*dashed lines* and *circles*), compared with those derived from experiment (*solid thick lines* and *squares*, data from (32)), showing good agreement, as demonstrated by the low values of $\langle \chi^2 \rangle$, where the average is taken over all residues. To see this figure in color, go online.

quenching of photoactivated donors by the acceptors for short interdye separations. We find, however, that this effect is unlikely to be a significant factor in our simulations because the simulated transfer efficiencies are barely affected by excluding frames in which the dyes are in close proximity (Table S3).

Whereas the ensemble averages of R_g and R_{ee} are very similar, the distribution of R_{ee} for Aβ42 shows a significant shoulder at very short end-to-end distances, which is not seen for Aβ40. The distributions of R_g do not show such a feature for either peptide and behave as expected, with the longer peptide having a slightly larger size. The simplest interpretation of these effects is the presence of a small population of long-range contacts within the Aβ42 peptide without a global collapse that would affect the radius of gyration (see below). Our simulations are also in overall good agreement with NMR *J*-couplings and chemical shifts, which have been used to validate earlier MD studies. In Fig. 6 *D*, we show the $^3J_{\mathrm{HNH}\alpha}$ scalar couplings computed from the simulations with the Karplus equation (82) using a recent set of parameters (83), whereas Fig. S4 shows predicted chemical shifts. Although there are some localized discrepancies for certain residue types, probably reflecting residual force-field inaccuracies, both *J*-couplings and chemical shifts are generally in good agreement with experimental values from (32) (note that the RMSDs between the predicted and experimental chemical shifts are smaller than the prediction error of SPARTA+, ~1 ppm for both carbon shifts (84)). Importantly, our simulations are also consistent with estimates of the hydrodynamic radius of Aβ40 from diffusion measurements by NMR (1.73 ± 0.01 nm, as calculated using Hydropro (85), compared with the experimental value of 1.6 ± 0.1 nm (86)), which confirms that the overall dimensions of the protein are reasonable.

Having shown that the simulations are able to recapitulate experimental observations, we sought to explain the differences in the R_{ee} distributions at a residue-level by performing a contact analysis. The ensemble-averaged intramolecular contact maps (Fig. 7 *B*) reveal a nearly complete absence of long-range contacts, suggesting that these peptides are almost entirely disordered. We have characterized this disorder by fitting an approximate scaling exponent to the mean intramolecular distances $r_{|i-j|}$ (Fig. 7 *A*) as a function of their sequence separation $|i-j|$. Indeed, the fitted scaling exponents of $\nu = 0.5197 \pm 0.0006$ and 0.5180 ± 0.0004, respectively, for Aβ40 and Aβ42, indicate that both peptides are close to the Θ-state in which attractive interactions approximately balance repulsive excluded volume interactions. A similar conclusion was reached from analysis of FRET data for a number of unfolded and intrinsically disordered proteins under folding conditions (87), suggesting that Aβ has global properties typical of other disordered proteins. Because structured species with low population may still be lost in such an average, we also examined in more detail the contact maps of individual structures. We partitioned the conformational ensemble of each peptide into clusters of structures with similar features in the contact map, using the *k*-means machine learning algorithm, which we optimized to avoid overfitting and validated as being robust in cluster assignment despite its stochastic mechanism (see Fig. S5; Table S4). As expected, and most significantly, we find that the vast majority of the ensemble populated by both peptides is completely devoid of any long-range contacts or appreciable structure (Fig. 7, *C* and *D*); the major clusters for both peptides show featureless average intramolecular contact maps, and the most representative structures are largely random coil, save for short stretches of helix in the Aβ42 cluster center that are unlikely to be significant (and definitely do not account for the shoulder in the distribution of R_{ee} in Fig. 6 *B*). This random coil subpopulation accounts for the majority (70.1 and 71.6%, respectively, for Aβ40 and Aβ42) of the sampled ensembles, indicating that neither peptide is subject to a strong drive toward folding, as expected for an IDP and in agreement with the average contact maps. The secondmost populated clusters observed are still largely disordered, as evident from the contact maps, but include some short-range contacts between residues, with the largest sequence separation of contacting residues being ~5. For Aβ40, these contacts are between residues located in the loop of the fibril structures, specifically between D23 and K28 (this same pair of residues interact as an intermolecular salt bridge in solid-state NMR fibril structures of Aβ40 (5,13), and was also observed in earlier MD studies), whereas for Aβ42, the main contacts are in the N-terminus, between the two aromatic residues Y10 and F4. These locally structured states account, respectively, for 27.6 and 25.6% of the Aβ40 and Aβ42 ensembles, but have FRET efficiencies (0.70 and 0.72, respectively) very similar to the ensemble averages.

The smallest clusters (2.3 and 2.8%, respectively, for Aβ40 and Aβ42) of both peptides show more extensive contact formation. The central structure of this cluster for Aβ40 shows the formation of several locally structured regions, with the maximum sequence-separation of contacts being ~15 residues. In contrast, Aβ42 forms long-range β-sheet between N- and C-termini involving hydrogen bonding of backbone atoms of G38, V39, V40, and I41 with F4, E3, A2, and D1, with the C-terminal A42 excluded from the motif perhaps due to electrostatic clashes between the charged carboxyl terminus and the side chains of the N-terminal residues D1 and E3 (see Fig. S6 *B*). This N- to C-terminal strand formation results in a very low end-to-end distance, thereby explaining the low-R_{ee} probability shoulder of the Aβ42 distribution in Fig. 6 *B*, and may help to explain the marginally higher experimentally observed FRET efficiency of freely diffusing Aβ42. This interterminal contact was observed independently in several

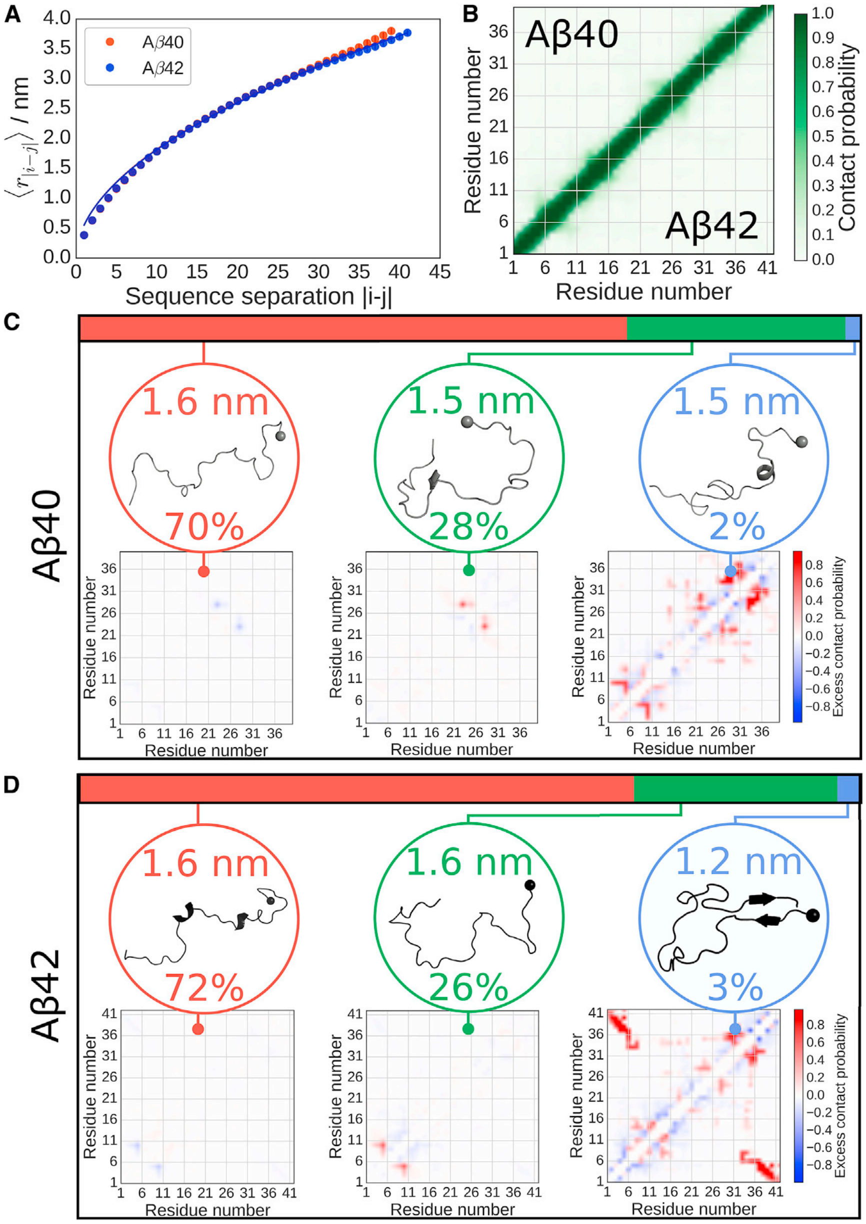

FIGURE 7 Conformational ensembles of Aβ40 and Aβ42. (*A*) Internal Cα atom distance scalings for each peptide, with data shown as circles, and fits to a power law as described in the Supporting Material as solid lines, giving scaling exponents of $\nu = 0.5197 \pm 0.0006$ and 0.5180 ± 0.0004, respectively, for Aβ40 and Aβ42. Note that the similarity in peptide behaviors means that the fitted curve for Aβ40 overlaps with that of Aβ42. (*B*) Simulation-averaged intramolecular contact maps show no significant secondary structure for either peptide, with Aβ40 shown in the upper half and Aβ42 in the lower. (*C*) Major clusters for the structural ensemble of Aβ40. The top colored bar denotes the observed statistical weights of each subpopulation, for which the most representative structure (with the N-terminus denoted by a *sphere*) and average intramolecular contact map relative to the ensemble-averaged contact map are shown. Blue contacts are those populated less frequently than the average, whereas red are those populated more frequently. The average radius of gyration and population for each cluster are shown accompanying the structure. The first cluster is random coil, the second populates very local contacts, and the last shows structure within the termini. (*D*) Major clusters for the structural ensemble of Aβ42. Similarly to the Aβ40 ensemble, the first cluster is random coil and the second populates very local contacts, whereas the last shows the structure formation between the termini. To see this figure in color, go online.

different REMD windows, and was reversible on the timescale of the simulations (Fig. S7). Nevertheless, because of the low population of this structure, and limitations of current force fields and conformational sampling, we conducted a similar analysis on a completely separate set of REMD simulations performed with a different force field (Amber ff03ws). This force field differs from Amber ff99SBws in both the atomic partial charges and the backbone and side-chain torsion angle potentials, although both force fields have been shown to yield reasonable properties for disordered proteins (43). This force field yielded values of the peptide FRET efficiencies and NMR signals consistent with those obtained using ff99SBws (Fig. S8). Remarkably, we find a very similar picture (Fig. S9), with the same β-structure forming between the termini of Aβ42, but not Aβ40, lending confidence to our interpretation. We also note that there are no contacts between these residues in the structures used to initialize the simulations (*contact maps* shown in Fig. S10, *A*–D), confirming that they were formed independently during the course of the two simulations. Why, then, is the short β-sheet formed between the N- and C-termini in Aβ42 not observed in Aβ40, given the extremely high sequence similarity? One possible reason is that, in the shorter isoform, the terminal V40 would carry the C-terminal charge, which would interact unfavorably with residues D1 and E3. It would also be difficult to form a sheet with a shift of register due to the presence of glycine residues at positions 37 and

38, as this residue disfavors formation of secondary structure.

CONCLUSIONS

A large body of experimental and simulation studies has considered the structure of monomeric Aβ, as this is the starting point for the formation of all Aβ amyloid fibrils, with many of these studies inferring a substantial population of structured species. Although our experimental results cannot rule out such structured species, the timescale of their formation or breaking would have to be <1 μs, which is shorter than the folding time of the fastest-folding β-hairpins (88), making it unlikely. An alternative possibility is that these stable states have a similar FRET efficiency as the average of the unstructured states. The most probable interpretation of the data, including urea denaturation, 2D FRET efficiency-lifetime analysis, and FCS measurements, however, is that the peptides populate a broad ensemble of structures interconverting on a timescale of tens of nanoseconds, as is typical for disordered proteins. Our simulations, which are in excellent agreement with experiment, provide a consistent picture in which the vast majority of conformations are disordered, or form only local structure. Intriguingly, we do observe a very small population ($\sim$3%) of β-structure formed between the termini of Aβ42 only, which may explain its slightly higher experimental FRET efficiency. The main difference from earlier simulations, which also predicted a population of disordered states, is that the population of collapsed and structured states is extremely small in our simulations; earlier results also suggested a smaller average radius of gyration of 1.0–1.2 nm (38,86). It is unlikely that structures with such a low R_g could be consistent with the FRET experiments reported here. Those simulations were nonetheless in agreement with NMR data such as NMR *J* couplings, NOEs, and chemical shifts that primarily reflect local structure formation. The new FRET data, although not as detailed as from NMR, therefore provide us with a more powerful discriminating factor between different simulation ensembles through constraints on global peptide behavior.

What is the relation, if any, between monomer structure and the different rates of primary nucleation for these two peptides? One may speculate that the formation of β-structure between the termini of Aβ42 reduces the entropic cost for formation of subsequent ordered species, leading to the experimentally observed higher nucleation rate (17). Overall, however, the similarity in properties between the two peptides, and lack of stable structure in either, suggests that monomer structure alone is unlikely to play the deciding role in the nucleation differences, consistent with the nucleated conformational conversion model of amyloid fibril formation (53,89–92), but that, instead, the effect possibly arises from enhanced intermolecular interactions due to the additional two hydrophobic C-terminal residues.

SUPPORTING MATERIAL

Supporting Materials and Methods, ten figures, and four tables are available at http://www.biophysj.org/biophysj/supplemental/S0006-3495(17)35128-7.

AUTHOR CONTRIBUTIONS

F.M., M.M.J.B., R.B.B., and H.S.C. designed research and wrote the manuscript. F.M. performed experiments and analyzed experimental data. M.M.J.B. performed MD simulations and analyzed simulation data. J.-Y.K. contributed analytic tools. G.H.Z. analyzed simulation data.

ACKNOWLEDGMENTS

We thank I. V. Gopich and B. Schuler for very helpful suggestions and comments on the nsFCS experiment and analysis; R. Tycko, W. A. Eaton, and A. Szabo, for numerous helpful discussions and comments; P. G. Schultz for sharing the plasmid for the expression and incorporation of an unnatural amino acid 4-acetyl phenylalanine; J. Roche for providing carbon chemical shift data; and J. M. Louis for advice and suggestions on protein expression and purification. This work utilized the high performance computational capabilities of the Biowulf Linux cluster at the National Institutes of Health (NIH), Bethesda, MD (http://biowulf.nih.gov).

This work was supported by the Intramural Research Program of the National Institute of Diabetes and Digestive and Kidney Diseases (NIDDK), National Institutes of Health (NIH). M.M.J.B. was supported by the NIH-Oxford/Cambridge Scholars Program and the Cambridge Commonwealth, European and International Trust.

SUPPORTING CITATIONS

References (93–104) appear in the Supporting Material.

REFERENCES

1. Selkoe, D. J. 2011. Alzheimer's disease. *Cold Spring Harb. Perspect. Biol.* 3:a004457.
2. Kirschner, D. A., C. Abraham, and D. J. Selkoe. 1986. X-ray diffraction from intraneuronal paired helical filaments and extraneuronal amyloid fibers in Alzheimer disease indicates cross-β conformation. *Proc. Natl. Acad. Sci. USA.* 83:503–507.
3. Malinchik, S. B., H. Inouye, …, D. A. Kirschner. 1998. Structural analysis of Alzheimer's β(1–40) amyloid: protofilament assembly of tubular fibrils. *Biophys. J.* 74:537–545.
4. Tycko, R. 2011. Solid-state NMR studies of amyloid fibril structure. *Annu. Rev. Phys. Chem.* 62:279–299.
5. Petkova, A. T., W.-M. Yau, and R. Tycko. 2006. Experimental constraints on quaternary structure in Alzheimer's β-amyloid fibrils. *Biochemistry.* 45:498–512.
6. Paravastu, A. K., R. D. Leapman, …, R. Tycko. 2008. Molecular structural basis for polymorphism in Alzheimer's β-amyloid fibrils. *Proc. Natl. Acad. Sci. USA.* 105:18349–18354.
7. Lu, J.-X., W. Qiang, …, R. Tycko. 2013. Molecular structure of β-amyloid fibrils in Alzheimer's disease brain tissue. *Cell.* 154:1257–1268.
8. Xiao, Y., B. Ma, …, Y. Ishii. 2015. Aβ(1–42) fibril structure illuminates self-recognition and replication of amyloid in Alzheimer's disease. *Nat. Struct. Mol. Biol.* 22:499–505.
9. Wälti, M. A., F. Ravotti, …, R. Riek. 2016. Atomic-resolution structure of a disease-relevant Aβ(1–42) amyloid fibril. *Proc. Natl. Acad. Sci. USA.* 113:E4976–E4984.

10. Colvin, M. T., R. Silvers, …, R. G. Griffin. 2016. Atomic resolution structure of monomorphic Aβ42 amyloid fibrils. *J. Am. Chem. Soc.* 138:9663–9674.
11. Petkova, A. T., R. D. Leapman, …, R. Tycko. 2005. Self-propagating, molecular-level polymorphism in Alzheimer's β-amyloid fibrils. *Science.* 307:262–265.
12. Tycko, R. 2015. Amyloid polymorphism: structural basis and neurobiological relevance. *Neuron.* 86:632–645.
13. Tycko, R., and R. B. Wickner. 2013. Molecular structures of amyloid and prion fibrils: consensus versus controversy. *Acc. Chem. Res.* 46:1487–1496.
14. Qiang, W., W.-M. Yau, …, R. Tycko. 2017. Structural variation in amyloid-β fibrils from Alzheimer's disease clinical subtypes. *Nature.* 541:217–221.
15. Knowles, T. P. J., M. Vendruscolo, and C. M. Dobson. 2014. The amyloid state and its association with protein misfolding diseases. *Nat. Rev. Mol. Cell Biol.* 15:384–396.
16. Cohen, S. I. A., S. Linse, …, T. P. J. Knowles. 2013. Proliferation of amyloid-β42 aggregates occurs through a secondary nucleation mechanism. *Proc. Natl. Acad. Sci. USA.* 110:9758–9763.
17. Meisl, G., X. Yang, …, T. P. J. Knowles. 2014. Differences in nucleation behavior underlie the contrasting aggregation kinetics of the Aβ40 and Aβ42 peptides. *Proc. Natl. Acad. Sci. USA.* 111:9384–9389.
18. Bitan, G., M. D. Kirkitadze, …, D. B. Teplow. 2003. Amyloid β-protein (Aβ assembly: Aβ 40 and Aβ 42 oligomerize through distinct pathways. *Proc. Natl. Acad. Sci. USA.* 100:330–335.
19. Bernstein, S. L., N. F. Dupuis, …, M. T. Bowers. 2009. Amyloid-β protein oligomerization and the importance of tetramers and dodecamers in the aetiology of Alzheimer's disease. *Nat. Chem.* 1:326–331.
20. Haass, C., and D. J. Selkoe. 2007. Soluble protein oligomers in neurodegeneration: lessons from the Alzheimer's amyloid β-peptide. *Nat. Rev. Mol. Cell Biol.* 8:101–112.
21. Selkoe, D. J. 2008. Soluble oligomers of the amyloid β-protein impair synaptic plasticity and behavior. *Behav. Brain Res.* 192:106–113.
22. Larson, M. E., and S. E. Lesné. 2012. Soluble Aβ oligomer production and toxicity. *J. Neurochem.* 120 (*Suppl 1*):125–139.
23. Uversky, V. N. 2010. Mysterious oligomerization of the amyloidogenic proteins. *FEBS J.* 277:2940–2953.
24. Riek, R., P. Güntert, …, K. Wüthrich. 2001. NMR studies in aqueous solution fail to identify significant conformational differences between the monomeric forms of two Alzheimer peptides with widely different plaque-competence, Aβ(1–40)(ox) and Aβ(1–42)(ox). *Eur. J. Biochem.* 268:5930–5936.
25. Hou, L., H. Shao, …, M. G. Zagorski. 2004. Solution NMR studies of the Aβ(1-40) and Aβ(1-42) peptides establish that the Met35 oxidation state affects the mechanism of amyloid formation. *J. Am. Chem. Soc.* 126:1992–2005.
26. Yan, Y., and C. Wang. 2006. Aβ42 is more rigid than Aβ40 at the C terminus: implications for Aβ aggregation and toxicity. *J. Mol. Biol.* 364:853–862.
27. Yamaguchi, T., K. Matsuzaki, and M. Hoshino. 2011. Transient formation of intermediate conformational states of amyloid-β peptide revealed by heteronuclear magnetic resonance spectroscopy. *FEBS Lett.* 585:1097–1102.
28. Vivekanandan, S., J. R. Brender, …, A. Ramamoorthy. 2011. A partially folded structure of amyloid-β(1–40) in an aqueous environment. *Biochem. Biophys. Res. Commun.* 411:312–316.
29. Lazo, N. D., M. A. Grant, …, D. B. Teplow. 2005. On the nucleation of amyloid β-protein monomer folding. *Protein Sci.* 14:1581–1596.
30. Petkova, A. T., Y. Ishii, …, R. Tycko. 2002. A structural model for Alzheimer's β-amyloid fibrils based on experimental constraints from solid state NMR. *Proc. Natl. Acad. Sci. USA.* 99:16742–16747.
31. Fawzi, N. L., A. H. Phillips, …, T. Head-Gordon. 2008. Structure and dynamics of the Aβ(21–30) peptide from the interplay of NMR experiments and molecular simulations. *J. Am. Chem. Soc.* 130:6145–6158.
32. Roche, J., Y. Shen, …, A. Bax. 2016. Monomeric Aβ1–40 and Aβ1–42 peptides in solution adopt very similar Ramachandran map distributions that closely resemble random coil. *Biochemistry.* 55:762–775.
33. Ball, K. A., A. H. Phillips, …, T. Head-Gordon. 2011. Homogeneous and heterogeneous tertiary structure ensembles of amyloid-β peptides. *Biochemistry.* 50:7612–7628.
34. Ball, K. A., A. H. Phillips, …, T. Head-Gordon. 2013. Differences in β-strand populations of monomeric Aβ40 and Aβ42. *Biophys. J.* 104:2714–2724.
35. Sgourakis, N. G., Y. Yan, …, A. E. Garcia. 2007. The Alzheimer's peptides Aβ40 and 42 adopt distinct conformations in water: a combined MD/NMR study. *J. Mol. Biol.* 368:1448–1457.
36. Sgourakis, N. G., M. Merced-Serrano, …, A. E. Garcia. 2011. Atomic-level characterization of the ensemble of the Aβ(1–42) monomer in water using unbiased molecular dynamics simulations and spectral algorithms. *J. Mol. Biol.* 405:570–583.
37. Rosenman, D. J., C. R. Connors, …, A. E. García. 2013. Aβ monomers transiently sample oligomer and fibril-like configurations: ensemble characterization using a combined MD/NMR approach. *J. Mol. Biol.* 425:3338–3359.
38. Rosenman, D. J., C. Wang, and A. E. García. 2016. Characterization of Aβ monomers through the convergence of ensemble properties among simulations with multiple force fields. *J. Phys. Chem. B.* 120:259–277.
39. Lin, Y.-S., G. R. Bowman, …, V. S. Pande. 2012. Investigating how peptide length and a pathogenic mutation modify the structural ensemble of amyloid-β monomer. *Biophys. J.* 102:315–324.
40. Lin, Y.-S., and V. S. Pande. 2012. Effects of familial mutations on the monomer structure of Aβ_{42}. *Biophys. J.* 103:L47–L49.
41. Best, R. B. 2012. Atomistic molecular simulations of protein folding. *Curr. Opin. Struct. Biol.* 22:52–61.
42. Nettels, D., S. Müller-Späth, …, B. Schuler. 2009. Single-molecule spectroscopy of the temperature-induced collapse of unfolded proteins. *Proc. Natl. Acad. Sci. USA.* 106:20740–20745.
43. Best, R. B., W. Zheng, and J. Mittal. 2014. Balanced protein-water interactions improve properties of disordered proteins and non-specific protein association. *J. Chem. Theory Comput.* 10:5113–5124.
44. Piana, S., J. L. Klepeis, and D. E. Shaw. 2014. Assessing the accuracy of physical models used in protein-folding simulations: quantitative evidence from long molecular dynamics simulations. *Curr. Opin. Struct. Biol.* 24:98–105.
45. Piana, S., A. G. Donchev, …, D. E. Shaw. 2015. Water dispersion interactions strongly influence simulated structural properties of disordered protein states. *J. Phys. Chem. B.* 119:5113–5123.
46. Huang, J., S. Rauscher, …, A. D. MacKerell, Jr. 2017. CHARMM36m: an improved force field for folded and intrinsically disordered proteins. *Nat. Methods.* 14:71–73.
47. Dedmon, M. M., K. Lindorff-Larsen, …, C. M. Dobson. 2005. Mapping long-range interactions in α-synuclein using spin-label NMR and ensemble molecular dynamics simulations. *J. Am. Chem. Soc.* 127:476–477.
48. Salmon, L., G. Nodet, …, M. Blackledge. 2010. NMR characterization of long-range order in intrinsically disordered proteins. *J. Am. Chem. Soc.* 132:8407–8418.
49. Brustad, E. M., E. A. Lemke, …, A. A. Deniz. 2008. A general and efficient method for the site-specific dual-labeling of proteins for single molecule fluorescence resonance energy transfer. *J. Am. Chem. Soc.* 130:17664–17665.
50. Young, T. S., I. Ahmad, …, P. G. Schultz. 2010. An enhanced system for unnatural amino acid mutagenesis in *E. coli*. *J. Mol. Biol.* 395:361–374.
51. Soranno, A., B. Buchli, …, B. Schuler. 2012. Quantifying internal friction in unfolded and intrinsically disordered proteins with single-molecule spectroscopy. *Proc. Natl. Acad. Sci. USA.* 109:17800–17806.

52. Schuler, B., A. Soranno, …, D. Nettels. 2016. Single-molecule FRET spectroscopy and the polymer physics of unfolded and intrinsically disordered proteins. *Annu. Rev. Biophys.* 45:207–231.
53. Mukhopadhyay, S., R. Krishnan, …, A. A. Deniz. 2007. A natively unfolded yeast prion monomer adopts an ensemble of collapsed and rapidly fluctuating structures. *Proc. Natl. Acad. Sci. USA.* 104:2649–2654.
54. Best, R. B. 2017. Computational and theoretical advances in studies of intrinsically disordered proteins. *Curr. Opin. Struct. Biol.* 42:147–154.
55. Gopich, I. V., and A. Szabo. 2012. Theory of single-molecule FRET efficiency histograms. *Adv. Chem. Phys.* 146:245–297.
56. Chung, H. S., F. Meng, …, J. M. Louis. 2017. Oligomerization of the tetramerization domain of p53 probed by two- and three-color single-molecule FRET. *Proc. Natl. Acad. Sci. USA.* 114:E6812–E6821.
57. Hoffmann, A., D. Nettels, …, B. Schuler. 2011. Quantifying heterogeneity and conformational dynamics from single molecule FRET of diffusing molecules: recurrence analysis of single particles (RASP). *Phys. Chem. Chem. Phys.* 13:1857–1871.
58. Schuler, B., E. A. Lipman, and W. A. Eaton. 2002. Probing the free-energy surface for protein folding with single-molecule fluorescence spectroscopy. *Nature.* 419:743–747.
59. Sherman, E., and G. Haran. 2006. Coil-globule transition in the denatured state of a small protein. *Proc. Natl. Acad. Sci. USA.* 103:11539–11543.
60. Merchant, K. A., R. B. Best, …, W. A. Eaton. 2007. Characterizing the unfolded states of proteins using single-molecule FRET spectroscopy and molecular simulations. *Proc. Natl. Acad. Sci. USA.* 104:1528–1533.
61. Hoffmann, A., A. Kane, …, B. Schuler. 2007. Mapping protein collapse with single-molecule fluorescence and kinetic synchrotron radiation circular dichroism spectroscopy. *Proc. Natl. Acad. Sci. USA.* 104:105–110.
62. Ziv, G., D. Thirumalai, and G. Haran. 2009. Collapse transition in proteins. *Phys. Chem. Chem. Phys.* 11:83–93.
63. Müller-Späth, S., A. Soranno, …, B. Schuler. 2010. From the cover: charge interactions can dominate the dimensions of intrinsically disordered proteins. *Proc. Natl. Acad. Sci. USA.* 107:14609–14614.
64. Aznauryan, M., L. Delgado, …, B. Schuler. 2016. Comprehensive structural and dynamical view of an unfolded protein from the combination of single-molecule FRET, NMR, and SAXS. *Proc. Natl. Acad. Sci. USA.* 113:E5389–E5398.
65. Zheng, W., A. Borgia, …, R. B. Best. 2016. Probing the action of chemical denaturant on an intrinsically disordered protein by simulation and experiment. *J. Am. Chem. Soc.* 138:11702–11713.
66. Borgia, A., W. Zheng, …, B. Schuler. 2016. Consistent view of polypeptide chain expansion in chemical denaturants from multiple experimental methods. *J. Am. Chem. Soc.* 138:11714–11726.
67. Chung, H. S., K. McHale, …, W. A. Eaton. 2012. Single-molecule fluorescence experiments determine protein folding transition path times. *Science.* 335:981–984.
68. Chung, H. S., T. Cellmer, …, W. A. Eaton. 2013. Measuring ultrafast protein folding rates from photon-by-photon analysis of single molecule fluorescence trajectories. *Chem. Phys.* 422:229–237.
69. Chung, H. S., and I. V. Gopich. 2014. Fast single-molecule FRET spectroscopy: theory and experiment. *Phys. Chem. Chem. Phys.* 16:18644–18657.
70. Grant, M. A., N. D. Lazo, …, D. B. Teplow. 2007. Familial Alzheimer's disease mutations alter the stability of the amyloid β-protein monomer folding nucleus. *Proc. Natl. Acad. Sci. USA.* 104:16522–16527.
71. Gopich, I. V., and A. Szabo. 2009. Decoding the pattern of photon colors in single-molecule FRET. *J. Phys. Chem. B.* 113:10965–10973.
72. Sisamakis, E., A. Valeri, …, C. A. M. Seidel. 2010. Accurate single-molecule FRET studies using multiparameter fluorescence detection. *Methods Enzymol.* 475:455–514.
73. Kalinin, S., A. Valeri, …, C. A. M. Seidel. 2010. Detection of structural dynamics by FRET: a photon distribution and fluorescence lifetime analysis of systems with multiple states. *J. Phys. Chem. B.* 114:7983–7995.
74. Gopich, I. V., and A. Szabo. 2012. Theory of the energy transfer efficiency and fluorescence lifetime distribution in single-molecule FRET. *Proc. Natl. Acad. Sci. USA.* 109:7747–7752.
75. Chung, H. S., J. M. Louis, and I. V. Gopich. 2016. Analysis of fluorescence lifetime and energy transfer efficiency in single-molecule photon trajectories of fast-folding proteins. *J. Phys. Chem. B.* 120:680–699.
76. Schuler, B., and W. A. Eaton. 2008. Protein folding studied by single-molecule FRET. *Curr. Opin. Struct. Biol.* 18:16–26.
77. Nettels, D., I. V. Gopich, …, B. Schuler. 2007. Ultrafast dynamics of protein collapse from single-molecule photon statistics. *Proc. Natl. Acad. Sci. USA.* 104:2655–2660.
78. Nettels, D., A. Hoffmann, and B. Schuler. 2008. Unfolded protein and peptide dynamics investigated with single-molecule FRET and correlation spectroscopy from picoseconds to seconds. *J. Phys. Chem. B.* 112:6137–6146.
79. Gopich, I. V., D. Nettels, …, A. Szabo. 2009. Protein dynamics from single-molecule fluorescence intensity correlation functions. *J. Chem. Phys.* 131:095102.
80. Chung, H. S., J. M. Louis, and W. A. Eaton. 2009. Experimental determination of upper bound for transition path times in protein folding from single-molecule photon-by-photon trajectories. *Proc. Natl. Acad. Sci. USA.* 106:11837–11844.
81. Acharya, S., K. R. Srivastava, …, L. J. Lapidus. 2016. Monomer dynamics of Alzheimer peptides and kinetic control of early aggregation in Alzheimer's disease. *ChemPhysChem.* 17:3470–3479.
82. Karplus, M. 1959. Contact electron-spin coupling of nuclear magnetic moments. *J. Chem. Phys.* 30:11–15.
83. Vögeli, B., J. Ying, …, A. Bax. 2007. Limits on variations in protein backbone dynamics from precise measurements of scalar couplings. *J. Am. Chem. Soc.* 129:9377–9385.
84. Shen, Y., and A. Bax. 2010. SPARTA+: a modest improvement in empirical NMR chemical shift prediction by means of an artificial neural network. *J. Biomol. NMR.* 48:13–22.
85. Ortega, A., D. Amorós, and J. García de la Torre. 2011. Prediction of hydrodynamic and other solution properties of rigid proteins from atomic- and residue-level models. *Biophys. J.* 101:892–898.
86. Granata, D., F. Baftizadeh, …, M. Vendruscolo. 2015. The inverted free energy landscape of an intrinsically disordered peptide by simulations and experiments. *Sci. Rep.* 5:15449.
87. Hofmann, H., A. Soranno, …, B. Schuler. 2012. Polymer scaling laws of unfolded and intrinsically disordered proteins quantified with single-molecule spectroscopy. *Proc. Natl. Acad. Sci. USA.* 109:16155–16160.
88. Kubelka, J., J. Hofrichter, and W. A. Eaton. 2004. The protein folding 'speed limit'. *Curr. Opin. Struct. Biol.* 14:76–88.
89. Serio, T. R., A. G. Cashikar, …, S. L. Lindquist. 2000. Nucleated conformational conversion and the replication of conformational information by a prion determinant. *Science.* 289:1317–1321.
90. Vitalis, A., and R. V. Pappu. 2011. Assessing the contribution of heterogeneous distributions of oligomers to aggregation mechanisms of polyglutamine peptides. *Biophys. Chem.* 159:14–23.
91. Lee, J., E. K. Culyba, …, J. W. Kelly. 2011. Amyloid-β forms fibrils by nucleated conformational conversion of oligomers. *Nat. Chem. Biol.* 7:602–609.
92. Šarić, A., Y. C. Chebaro, …, D. Frenkel. 2014. Crucial role of nonspecific interactions in amyloid nucleation. *Proc. Natl. Acad. Sci. USA.* 111:17869–17874.
93. Zheng, Q., S. Jockusch, …, S. C. Blanchard. 2014. The contribution of reactive oxygen species to the photobleaching of organic fluorophores. *Photochem. Photobiol.* 90:448–454.

94. Zheng, Q., M. F. Juette, …, S. C. Blanchard. 2014. Ultra-stable organic fluorophores for single-molecule research. *Chem. Soc. Rev.* 43:1044–1056.

95. Páll, S., M. J. Abraham, …, E. Lindahl. 2015. Tackling exascale software challenges in molecular dynamics simulations with GROMACS. *In* Lecture Notes in Computer Science. Springer, Cham, Switzerland, pp. 3–27.

96. Abascal, J. L. F., and C. Vega. 2005. A general purpose model for the condensed phases of water: TIP4P/2005. *J. Chem. Phys.* 123:234505.

97. Parrinello, M., and A. Rahman. 1981. Polymorphic transitions in single crystals: a new molecular dynamics method. *J. Appl. Phys.* 52:7182–7190.

98. Nosé, S., and M. L. Klein. 1983. Constant pressure molecular dynamics for molecular systems. *Mol. Phys.* 50:1055–1076.

99. Essmann, U., L. Perera, …, L. G. Pedersen. 1995. A smooth particle mesh Ewald method. *J. Chem. Phys.* 103:8577–8593.

100. Hess, B., H. Bekker, …, J. G. E. M. Fraaije. 1997. LINCS: a linear constraint solver for molecular simulations. *J. Comput. Chem.* 18:1463–1472.

101. Graen, T., M. Hoefling, and H. Grubmüller. 2014. AMBER-DYES: characterization of charge fluctuations and force field parameterization of fluorescent dyes for molecular dynamics simulations. *J. Chem. Theory Comput.* 10:5505–5512.

102. Kabsch, W., and C. Sander. 1983. Dictionary of protein secondary structure: pattern recognition of hydrogen-bonded and geometrical features. *Biopolymers.* 22:2577–2637.

103. Kjaergaard, M., S. Brander, and F. M. Poulsen. 2011. Random coil chemical shift for intrinsically disordered proteins: effects of temperature and pH. *J. Biomol. NMR.* 49:139–149.

104. Kjaergaard, M., and F. M. Poulsen. 2011. Sequence correction of random coil chemical shifts: correlation between neighbor correction factors and changes in the Ramachandran distribution. *J. Biomol. NMR.* 50:157–165.

Biophysical Journal, Volume *114*

Supplemental Information

Highly Disordered Amyloid-β Monomer Probed by Single-Molecule FRET and MD Simulation

Fanjie Meng, Mathias M.J. Bellaiche, Jae-Yeol Kim, Gül H. Zerze, Robert B. Best, and Hoi Sung Chung

SI Materials, Methods, and Theory

Protein expression and incorporation of an unnatural amino acid. The amino acid sequences of Aβ40 and Aβ42 are shown in Fig. 1. For site-specific labeling of the donor (Alexa 488) and acceptor (Alexa 647) dyes, an unnatural amino acid, 4-acetylphenylalanine (Synchem, Elk Grove Village, IL) and a cysteine residue were attached to the N- and C-terminus of Aβ, respectively (UA-Aβ40-C and UA-Aβ42-C). For the incorporation of 4-acetylphenylalanine, we used an amber codon TAG. We prepared two protein constructs for both Aβ40 and Aβ42. To immobilize proteins on a biotin-embedded glass coverslip, a biotin accepting sequence (AviTag, Avidity LLC, Aurora, Colorado) and a flexible linker sequence were attached to the N-terminus of Aβ (Avi-UA-Aβ40-C and Avi-UA-Aβ42-C). The DNA sequences of UA-Aβ42-C and Avi-UA-Aβ42-C are `ATGGGTATGAGCTAGGACGCTGAGTTCAGGCACGACTCTGGTTATGAAGTACACCACCAGAAACTGGTTTTCTTTGCAGAAGATGTAGGTTCAAATAAAGGAGCAATTATTGGCCTGATGGTGGGTGGTGTCGTGATTGCGTGCTAA` and `ATGGGTATGAGCGGTCTGAATGATATCTTTGAGGCGCAAAAGATTGAGTGGCACGAGTCCTCCGGTCTGGTCGCGGGTGGTGGCGGCTCTGGCGGCGGCGGCAGCGGTGGCGGCGGCTCGTAGGACGCTGAGTTCAGGCACGACTCTGGTTATGAAGTACACCACCAGAAACTGGTTTTCTTTGCAGAAGATGTAGGTTCAAATAAAGGAGCAATTATTGGCCTGATGGTGGGTGGTGTCGTGATTGCGTGCTAA`, respectively. The codons for unnatural amino acid (TAG), cysteine (TGC) and AviTag are underlined. The DNA sequences of UA-Aβ40-C and Avi-UA-Aβ40-C do not contain the two C-terminal residues (ATTGCG). All four plasmids were constructed by DNA2.0 (DNA2.0, Neward, CA). The pEVOL plasmid (1) encodes an evolved amino acetyl-tRNA synthetase and a suppressor tRNA_{CUA} to incorporate 4-acetylphenylalanine. To ensure the expression of biotinylated proteins, we co-expressed the BirA gene to generate sufficient biotin ligase (Avidity LLC).

We co-transformed *E. coli* strain BL-21 (DE3) (Stratagene, La Jolla, CO) with chloramphenicol-resistant pEVOL, kanamycin-resistant pJ411-BirA, and carbenicillin-resistant pJ414-Aβ, for the expression of Avi-Aβ constructs. For the constructs without AviTag, we co-transformed bacteria with pEVOL and pJ414-Aβ. The expression level of the full-length protein was optimized by varying the ratio of the plasmids because most of the expression was truncated at the TAG site. The optimized condition was 0.6 μL of pEVOL (50 ng/μL), 0.2 μL of pJ411-BirA (50 ng/μL) and 0.2 μL of a protein construct (20 ng/μL). Co-transformed bacteria were spread on LB-agar plates with corresponding antibiotics. After incubation at 37°C overnight, 2 - 3 individual colonies were picked and inoculated in 5 mL LB broth with the same antibiotics combinations for 16-24 hours at 37°C with shaking at 250 rpm. Colonies grown up in liquid medium were diluted into the same medium of 500 - 1000 mL for further growth. After incubation for 6 - 8 hours, expression was induced at OD 0.6 (600 nm) with final concentrations of 1 mM IPTG, 1 mM arabinose, 1 mM 4-acetylphenylalanine and 50 μM *d*-biotin. After overnight incubation at 25°C with shaking at 250 rpm, bacteria was harvested and spun down at 8000 g for 10 minutes using Sorvall LYNX 4000 centrifuge (Thermo Scientific, Waltham, MA). After removing the supernatant, pellets were either used for lysis right away or frozen at - 20°C for future use.

Purification of Aβ40 and Aβ42. Bacteria pellets from 500 mL LB culture were lysed in 20 mL of bacterial protein extraction reagent (B-Per, Thermo Fisher Scientific, Grand Island, NY) with 50 mM benzamidine hydrochloride, 100 μg/mL lysozyme (Sigma, St. Louis, MO), and 5 units of benzonase (Novogen, Madison, WI). The pellets were mixed and re-suspended in the lysis buffer and incubated at room temperature for 30 minutes. The lysate was transferred to 50 mL spinning tubes and centrifuged at 30000 g for 45 minutes with Sorvall LYNX 4000. The supernatant was removed for electrophoresis and the pellet containing inclusion bodies were re-suspended in 30 mL 1× PBS solution with 10 mM DTT and 1% Triton X-100 and sonicated three times for 20 seconds on ice using a sonicator at 100% power (Model Q55, Qsonica, Newtown, CT). The solution was then centrifuged at 30000 g for 30 minutes at 4°C. The supernatant was discarded and the remaining pellet was re-suspended in the same PBS buffer used in the previous sonication step with 1 M sodium chloride to remove DNA and RNA from pellets. The mixture was sonicated as the previous step and centrifuged at 30000 g for 30 minutes at 4°C. Re-suspension, sonication, and centrifugation were repeated in 1× PBS. The pellet containing inclusion bodies was dissolved in 5 mL of 50 mM Tris-HCl with 6 M guanidine hydrochloride (GdmCl) and 10 mM DTT, and kept at room temperature overnight for complete dissolution of proteins. The solution was centrifuged at 30000 g for 45 minutes at 4°C to remove the insoluble pellet and collect the supernatant for further purification. The supernatant was loaded on PhastSystem (Pharmacia, Baltimore, MD) gels. Gels were stained with Phastgel Blue R (Pharmacia, Baltimore, MD) then washed until protein bands were clearly shown. Aβ proteins with and without AviTag and linker appear at 8 kDa and 5 kDa on gels, respectively, and these are the smallest proteins in the inclusion body. 500 μL of protein solutions were loaded onto the AKTA pure FPLC system equipped with a Superdex^{TM}75 10/300GL size exclusion column (GE Healthcare, Chicago, IL). The separation was run with 50 mM Tris-HCl, 4 M GdmCl solution at a flow rate of 0.8 mL/min. The fractions containing 5 kDa or 8 kDa proteins identified by Phastgel were collected and concentrated using Amicon Ultra centrifugal filters (EMD Millipore, Billerica, MA) and then subjected to second round of FPLC purification.

Dye labeling and purification. We first labeled 4-acetylphenylalanine with Alexa Fluor 488 (Alexa 488) hydroxylamine (A30629, Thermo Fisher Scientific, Carlsbad, CA). Aβ (~ 0.2 mg) in 4 M GdmCl solution was exchanged and concentrated to 100 μL in 6 M GdmCl in acetate buffer at pH 4.0 using Amicon centrifugal filters. 100 μL of a protein solution was mixed with 0.1 mg of Alexa 488 hydroxylamine pre-dissolved in 5 μL of DMSO. To promote the reaction, we incubated the mixture at 37°C overnight. The reaction was quenched by adding 4 μL of β-mercaptoethanol and 30 μL of 1 M Tris-HCl, pH 8.0. The reaction mixture was fractionated on a Superdex^{TM}75 10/300GL size exclusion column equilibrated with 50 mM Tris-HCl, pH 8.0, 4 M GdmCl to remove the excess free dye. The fraction containing labeled proteins was concentrated and incubated at room temperature for 1 – 2 hours in the presence of 1.5 mM tris (2-carboxyethyl) phosphine (TCEP) to fully reduce the cysteine residue. TCEP was removed by exchanging buffer into 50 mM Tris-HCl, pH 7.0, 6 M GdmCl and the sample was concentrated to 100 μL. To label cysteine with Alexa Fluor 647 maleimide (Alexa 647, A20347, Thermo Fisher Scientific, Carlsbad, CA), the solution was incubated with 100 μg of Alexa 647 dissolved in 5 μL of DMSO at room temperature overnight. The reaction was quenched by adding 3 μL of β-mercaptoethanol and incubating the solution for 10 minutes. The mixture was loaded onto FPLC and separated with the superdex^{TM}75 10/300GL size exclusion column equilibrated with 50 mM Tris-HCl, pH 8.0, 4 M GdmCl. The peptide labeled with two dyes showed overlapping three peaks of absorbance monitored at 280, 494, and 651 nm. The labeled protein concentration was determined by the absorbance at 494 nm and 651 nm measured by Cary 8454 UV-Vis spectrophotometer (Agilent Technologies, Santa Clara, CA). Purified samples were aliquoted into 10 μL and kept at - 80°C for future experiments.

Single-molecule experiment. Single-molecule experiments were performed using a confocal microscope system (MicroTime200, Picoquant) with a 75 μm diam. pinhole, a dichroic beamsplitter (ZT405/488/635rpc, Chroma Technology), and an oil-immersion objective (UPLSAPO, NA 1.4, × 100, Olympus). In the free-diffusion experiment, solutions of 40 - 100 pM dye-labeled proteins were prepared in 50 mM 1× PBS, pH 7.5 at various urea concentrations. We added 0.01% Tween-20 to prevent sticking of proteins on a glass coverslip and 100 mM β-mercaptoethanol and 40 mM cysteamine to reduce blinking and bleaching of dyes (2). Alexa 488 was excited by a 485 nm diode laser (LDH-D-C-485, PicoQuant) in the continuous wave (CW) mode at 20 μW. Alexa 488 and Alexa 647 fluorescence was split into two channels using a beamsplitter (585DCXR, Chroma Technology) and focused through optical filters (ET525/50m for Alexa 488 and E600LP for Alexa 647, Chroma Technology) onto photon-counting avalanche photodiodes (SPCM-AQR-16, PerkinElmer Optoelectronics). Photons were collected into 2 ms bins for 1 to 2 hours and those containing 30 photons or more were considered as significant bursts for further analysis.

In the immobilization experiment, Aβ was immobilized on a biotin-embedded, PEG coated glass coverslip (Bio-01, Microsurfaces Inc., Englewood, NJ) as described previously (3). After being cleaned with deionized water and dried with a stream of nitrogen, the surface was covered with Cover well (PC8R-0.5) and pretreated with 20 μL streptavidin solution (25 μg/mL) for 5 minutes. The solution was replaced with 20 μL of 100 pM protein solution and checked on the microscope to monitor binding of proteins on the surface. After observing immobilization of a sufficient number of molecules (50 – 100 molecules per 10 x 10 μm^2), the solution was replaced with 1× PBS including a cocktail of 100 mM β-mercaptoethanol, 10 mM Cystamine, 2 mM 4-nitrobenzyl alcohol (NBA), 2 mM cyclooctatetraene (COT), and 2 mM Trolox (4, 5) to reduce photoblinking and photobleaching of dyes. For the study of the dynamics on the timescale from μs to ms, molecules were illuminated in the CW mode at 3 μW. For the fluorescence lifetime measurement, pulsed-mode excitation was used at the power of 0.3 μW.

All experiments were performed at room temperature (22ºC). Additional details of single-molecule experiments have been described elsewhere (6, 7, 3).

FRET efficiency and donor lifetime corrections in 2D FRET efficiency-lifetime analysis. 2D FRET efficiency-lifetime analysis performed in this study requires accurate values of the FRET efficiency and donor fluorescence lifetime. The mean FRET efficiency and donor delay time of the initial segment of each trajectory were calculated and corrected for various factors (8) including background, donor leak into the acceptor channel (cross-talk), ratio of the detection efficiencies and quantum yields of the donor and acceptor (γ-factor), direct acceptor excitation, and acceptor blinking. Although the details can be found in Ref. (6), we describe the correction procedures below briefly.

FRET efficiency corrections for background, donor leak, and γ-factor. The contribution of background photons is corrected by subtracting the background photon count rates from the mean photon count rates of corresponding detection channels for each segment. The background photon count rates were obtained from the segment after photobleaching of all dyes.

Donor leak into the acceptor channel, l can be measured as

$$l = n_A^0 \big/ (n_A^0 + n_D^0), \tag{S1}$$

where $n_A{}^0$ and $n_D{}^0$ are the background-corrected photon count rates in the acceptor and donor channels of a donor-only segment (no active acceptor). The count rates in the acceptor and donor channels of a segment with acceptor fluorescence are $n_A = n_A{}^c + ln_D{}^c$ and $n_D = (1 - l)n_D{}^c$, respectively, where $n_A{}^c$ and $n_D{}^c$ are the background and donor leak-corrected acceptor and donor count rates. The corrected count rates $n_A{}^c$ and $n_D{}^c$ can be calculated as

$$\begin{aligned} n_D^c &= n_D / (1 - l), \\ n_A^c &= n_A - n_D l / (1 - l) \end{aligned} \tag{S2}$$

The leak value averaged over the available trajectories is $l = 0.05$.

γ is the ratio of the detection efficiencies (η) and quantum yields (ϕ) of the acceptor and donor, $\gamma = (\eta_A\phi_A)/(\eta_D\phi_D)$. This factor can be determined experimentally by comparing the photon count rates of the segments before and after acceptor photobleaching as

$$\gamma = n_A^c \big/ (n_D^0 - n_D^c), \tag{S3}$$

where $n_A{}^c$ and $n_D{}^c$ are the background and donor-leak corrected count rates of the acceptor and donor before acceptor photobleaching and $n_D{}^0$ is that of the donor after acceptor photobleaching. The average γ values are 0.98 and 1.01 for the Aβ40 and Aβ42 experiments, respectively. The γ-corrected FRET efficiency is calculated as

$$E = n_A^c \big/ (n_A^c + \gamma n_D^c). \tag{S4}$$

A small fraction of acceptor count rate results from the direct acceptor excitation because of the weak absorption of the acceptor at the donor excitation wavelength (485 nm). This effect can be corrected together with the γ correction in Eq. S4 by using the γ value determined in Eq. S3 that is calculated from photon count rates including the contribution of direct acceptor excitation as shown in Ref. (6).

Determination and correction of donor fluorescence lifetime. We determined the donor lifetime from the mean donor delay time,

$$\tau_D = \langle \delta t_D \rangle - \delta t_{D0} - \tau_{IRF}^0, \tag{S5}$$

where $\langle \delta t_D \rangle$ is the average time delay of the donor photons from the laser trigger signal, δt_{D0} is the origin of the donor delay time, and τ_{IRF}^0 $(= \int_0^\infty tIRF(t)dt)$ is the mean delay time of the instrument response function (IRF) in the donor channel. IRF was measured using the reflected excitation light from a glass surface and fitted to the Gamma distribution (6, 9),

$$IRF(t) = \frac{k_\gamma}{\Gamma(a)}(k_\gamma t)^{a-1} e^{-k_\gamma t} \tag{S6}$$

where $\Gamma(a)$ is the Gamma function and a and k_γ are positive fitting parameters. δt_{D0} in Eq. S5 can be obtained by fitting the donor delay time distribution of the donor-only segments (no active acceptor) to the convolution of the IRF and a bi-exponential function as

$$P_D(\delta t) = \int_0^{\delta t} IRF(\delta t - \delta t_{D0} - t)[A_1\tau_1^{-1}\exp(-t/\tau_1) + A_2\tau_2^{-1}\exp(-t/\tau_2)]dt + B_D, \tag{S7}$$

where constant B_D is the background level in the donor channel. (The details of the calculation of Eq. S7 and fitting can be found in Ref. (6)) The average donor lifetime in the absence of the acceptor $\tau_D{}^0$ obtained by Eq. S5 is 3.1 ns.

Since the donor delay time is not affected by donor leak into the acceptor channel and acceptor direct excitation, it needs to be corrected only for background photons and acceptor blinking (6, 9). The uncorrected mean delay time (τ_D) including the contribution of background photons are related to the corrected mean delay time ($\tau_D{}^c$) as $(n_D + b_D)\tau_D = n_D\tau_D{}^c + b_D\tau_D{}^b$, where n_D is the background subtracted donor count rate, b_D and $\tau_D{}^b$ are the background photon count rate and the mean delay time of the background photons in the donor channel. Therefore, the contribution of background photons can be corrected as

$$\tau_D{}^c = [(n_D + b_D)\tau_D - b_D\tau_D{}^b] / n_D. \tag{S8}$$

The correction for acceptor blinking is described in the next section.

Maximum likelihood analysis of acceptor blinking. Donor blinking does not affect the FRET efficiency or lifetime because no photon is detected. However, these quantities are affected by acceptor blinking because only donor photons with long delay times are detected in the acceptor dark state. Since no apparent acceptor blinking is observed in the binned trajectories shown in Figs. 3 and 4, the timescale of the acceptor blinking must be shorter than the bin times. In this section, we describe how to extract acceptor blinking parameters using the maximum likelihood analysis of photon trajectories without binning and correct the FRET efficiency and donor lifetime in the immobilization experiment.

Determination of the acceptor bright state population using two-state maximum likelihood method. The likelihood function for a photon trajectory with records of photon colors and arrival times is (10)

$$L = \mathbf{1}^{\mathrm{T}} \prod_{i=2}^{N} \left[\mathbf{F}(c_i) \exp\left(\mathbf{K}(t_i - t_{i-1}) \right) \right] \mathbf{F}(c_1)\mathbf{p}_{eq}, \tag{S9}$$

where N is the number of photons in a trajectory, c_i is the color of the i^{th} photon (donor or acceptor), and t_i - $t_{i\text{-}1}$ is a time interval between the $(i\text{-}1)^{\text{th}}$ and i^{th} photons. **K** is the rate matrix, the photon color matrix **F** depends on the color c of a photon as **F**(*acceptor*) = **E** and **F**(*donor*) = **I** – **E**, where **E** is a diagonal matrix with the uncorrected FRET efficiencies of the individual states on the diagonal, **I** is the unity matrix, $\mathbf{1}^{\mathrm{T}}$ is the unit row vector (T means transpose), and $\mathbf{p}_{eq}$ is the vector of equilibrium populations. The parameters were determined by maximizing the likelihood function calculated by the diagonalization of **K** in Eq. S10 as described in Ref. (10).

For the two-state model, the matrix of FRET efficiencies, the rate matrix, and the vector of the equilibrium populations are given by

$$\boldsymbol{E} = \begin{pmatrix} E_1 & 0 \\ 0 & E_2 \end{pmatrix}, \ \mathbf{K} = \begin{pmatrix} -k_1 & k_2 \\ k_1 & -k_2 \end{pmatrix}, \ \mathbf{p}_{eq} = \begin{pmatrix} p_1 \\ 1 - p_1 \end{pmatrix}, \qquad \text{(S10)}$$

where k_1 (k_2) is the rate coefficient for the transition from state 1 to state 2 (state 2 to state 1) and $p_1 = k_2/(k_1 + k_2)$ is the equilibrium population of state 1. E_1 and E_2 are the apparent FRET efficiencies of state 1 and 2, respectively. The apparent FRET efficiency is the ratio of the acceptor count rate to the total count rate (including background photons). We performed the analysis with two different models. In the 2-state model without constraints in the FRET efficiency, there are four fitting parameters: E_1, E_2, k (= $k_1 + k_2$), and p_1. On the other hand, in the 1-state model with acceptor blinking, state 1 and 2 correspond to the bright and dark states of the acceptor, respectively. We define $k_1 = k_d$, $k_2 = k_b$, $p_1 = p_b$, $E_1 = E_b^{app}$, and $E_2 = E_d^{app}$. In this model, there are three fitting parameters: E_b^{app}, k_b, p_b. The FRET efficiency in the acceptor dark state E_d^{app} was fixed to be 0.06.

In the analysis of the data to probe potential dynamics on the μs – ms timescale (Fig. 3), parameters were extracted from the collective analysis of the entire data set instead of individual trajectories because the length of trajectories is much shorter than those for the 2D FRET efficiency-lifetime analysis due to the 10 times higher illumination intensity. In this case, when using the 1-state model with acceptor blinking, it is reasonable to assume that the rate coefficient for the transition from the bright state to the dark state of the acceptor, k_d, is proportional to the photon count rate while k_b is independent of the photon count rate because k_d increases linearly with the time spent in the excited state. Therefore, $k_d = k_d^0(n/n_0)$, where n is the average photon count rate of each photon trajectory and k_d^0 is the rate coefficient at the reference photon count rate (n_0 = 100 ms^{-1}). The bright state population is $p_b = k_b/(k_b + k_d)$. The parameters extracted using the 2-state model without constraints in the FRET efficiency and the 1-state model with acceptor blinking with a fixed E_d^{app} are compared in Table S2.

In the 2D FRET efficiency-lifetime analysis of the data collected at lower illumination intensity, each trajectory was corrected for acceptor blinking using the 1-state model with acceptor blinking (Fig. 4). In the acceptor dark state, photons are still detected in the acceptor channel because of donor leak and background noise; therefore, the uncorrected count rate in the acceptor channel is $(n - b_A - b_D)l + b_A$, where n is the uncorrected total photon count rate, b_A and b_D are the acceptor and donor background count rates, and l is the donor leak. Since the individual trajectories were analyzed separately, E_d^{app} was calculated for each trajectory to account for the slightly different background level as $E_d^{app} = [(n - b_A - b_D)l + b_A]/n$ and used in

Eq. S10. Fig. S1 *C* shows the bright state population p_b is ~ 0.95. Once p_b is determined for each segment, this value can be used to correct the FRET efficiency and mean donor delay time (lifetime) of each trajectory as described below.

FRET efficiency and lifetime corrections for acceptor blinking. The measured FRET efficiency (corrected for the γ-factor, Eq. S4) is $E = n_A/(n_A + \gamma n_D)$. The acceptor and donor count rates in the presence of acceptor blinking, n_A and n_D, can be expressed in terms of the acceptor bright state population p_b and the FRET efficiency when the acceptor is in the bright state, E^c, as follows. Since acceptor photons are emitted only when the acceptor is in the bright state, the acceptor photon count rate is $n_A = \gamma p_b n E^c$, where n is the background- and donor leak-corrected donor count rate in the absence of the energy transfer. Similarly, the donor count rate in the presence of the acceptor is $n_D = p_b n(1 - E^c) + (1 - p_b)n$, since donor photons are emitted from both bright and dark states of the acceptor. (We assume that there is no energy transfer from the donor to the acceptor in the acceptor dark state.) Using the above expressions for the count rates, we find that $E = p_b E^c$. Therefore, the FRET efficiency can be corrected for acceptor blinking by

$$E^c = E / p_b. \tag{S11}$$

The donor lifetime in the presence of acceptor blinking (τ_D) is the average of the donor lifetimes in the acceptor bright state (${\tau_D}^c$) and dark state (${\tau_D}^0$, donor lifetime in the absence of the acceptor) weighted by the donor count rate in each state as $[(1 - E^c)\, p_b + (1 - p_b)]n\,\tau_D = p_b n(1 - E^c)\,{\tau_D}^c + (1 - p_b)n\,{\tau_D}^0$. Note that τ_D is the background-corrected donor lifetime in Eq. S8. Then, the donor lifetime is corrected for acceptor blinking as

$${\tau_D}^c = \frac{(1-p_b E^c)\tau_D - (1-p_b)\tau_D^0}{p_b(1-E^c)}. \tag{S12}$$

FRET efficiency correction of free-diffusion data. To compare with the values obtained in the immobilization experiment, the FRET efficiency in the free-diffusion experiment was similarly corrected for background, donor leak, and γ-factor.

The FRET efficiency can be corrected for background photons as (8)

$$E = \frac{E^{app} n - b_A}{n - b_A - b_D}. \tag{S13}$$

Here, E^{app} is the apparent FRET efficiency obtained from the FRET efficiency distribution in Fig. 2, n is the average total photon count rate of fluorescence bursts including background photons, and b_A and b_D are the background count rates in the acceptor and donor channels, respectively. In order to obtain b_A and b_D, histograms of photon counts per 2 ms bin were constructed using the entire data set (not just fluorescence bursts) and the low count rate part (< 2 - 3 ms^{-1}) were fitted to the Poisson distribution. The background photon count rates were 0.3 – 0.5 ms^{-1} for both acceptor and donor channels.

The donor leak and γ-factor were corrected using l and γ values obtained from the immobilization experiment. The FRET efficiency values before and after the donor leak correction are $E = n_A/(n_A + n_D)$ and $E^c = n_A^c/(n_A^c + n_D^c)$, respectively. Using the relationship of the photon count rates in Eq. S2, one can correct the donor leak as

$$E^c = \frac{E-l}{1-l}. \tag{S14}$$

Similarly, γ-factor can be corrected using the relationship between the FRET efficiency before and after the correction as

$$E^c = \left(1+\gamma\left(1/E-1\right)\right)^{-1}. \tag{S15}$$

In Eq. S15, E is the FRET efficiency after the donor leak correction in Eq. S14.

Nanosecond fluorescence correlation spectroscopy (nsFCS). In the nsFCS experiments of Avi-Aβ40 and Avi-Aβ42, data were collected in the free-diffusion experiment mode described above at the protein concentration of 1 nM for 10 hours. Fluorescence emission was split by a 50/50 beamsplitter cube and donor and acceptor photons were further separated. The donor and acceptor auto-correlations and donor-acceptor cross correlation were obtained by constructing histograms of time intervals between all pairs of photons detected in different channels as described in Ref. (11, 12). The three correlation data from -2 to 2 μs were globally fitted to

$$C_{ij}(\tau) = A_{ij}(1-c_{AB}e^{-\tau/\tau_{AB}})(1+c_{CD}e^{-\tau/\tau_{CD}})(1+c_T e^{-\tau/\tau_T}), \quad i,j = A, D, \tag{S16a}$$

$$c_{CD} = \begin{cases} \dfrac{\langle n_D^2\rangle - \langle n_D\rangle^2}{\langle n_D\rangle^2} = \dfrac{\sigma_c{}^2}{E^2}, & \text{donor autocorrelation} \\ \dfrac{\langle n_A^2\rangle - \langle n_A\rangle^2}{\langle n_A\rangle^2} = \dfrac{\sigma_c{}^2}{\left(1-E\right)^2}, & \text{acceptor autocorrelation} \\ \dfrac{\langle n_D n_A\rangle - \langle n_D\rangle\langle n_A\rangle}{\langle n_D\rangle\langle n_A\rangle} = -\dfrac{\sigma_c{}^2}{E\left(1-E\right)}, & \text{cross-correlation} \end{cases}. \tag{S16b}$$

Here, A_{ij} is a normalization factor, τ_{AB}, τ_{CD}, and τ_T are the decay times by photon anti-bunching, conformational dynamics, and triplet blinking, respectively, and c_{AB}, c_{CD}, and c_T are the amplitudes of the corresponding components. n_A and n_D in Eq. S16b are acceptor and donor count rates and $\langle \ldots \rangle$ denotes an average over the conformational distribution. E is the true FRET efficiency after all corrections. The variance of the FRET efficiency distribution $\sigma_c{}^2$ can be obtained by globally fitting three correlation functions using the correlation amplitudes of the conformational dynamics c_{CD} in Eq. S16b (13, 3).

Correlation analysis of immobilization data. A donor-acceptor cross-correlation function of the data from the immobilization experiment was calculated as

$$C_{DA}(\tau) = \frac{\overline{\langle N_D(t+\tau) N_A(t) \rangle}}{\langle N_D \rangle \langle N_A \rangle} - 1 . \tag{S17}$$

N_D (t) and N_A (t) are the number of donor and acceptor photons in a bin at time t, $\langle \ldots \rangle$ is an average of a quantity in a given segment in a trajectory, and the upper bar indicates the average over segments. The correlation functions in Fig. 3C were calculated for the segments longer than 5 ms.

MD simulations. For each Aβ isoform, we ran temperature replica exchange molecular dynamics (T-REMD) simulations under isobaric-isothermal constraints using both the Amber ff03ws and Amber ff99SBws force fields (14), for 750 ns (Amber ff03ws), 743.760 ns (Amber ff99SBws, Aβ40) or 740.715 ns (Amber ff99SBws, Aβ42) using Gromacs version 4.6.7 (15). 40 temperature windows were used, ranging from T = 277 K to 355 K in steps of ΔT = 2 K, with swaps attempted between adjacent windows every 1 ps. Each system was explicitly solvated with TIP4P/2005 water (16) and 20 mM NaCl plus neutralizing cations.

Forces were evaluated every 2 fs using stochastic dynamics, propagated by integrating the Langevin equation of motion with a friction coefficient of 0.2 ps^{-1}. Isobaric constraints were imposed by using an isotropic Parrinello-Rahman barostat with coupling time constant 5 ps, reference pressure of 1 bar and compressibility 4.5×10^{-5} bar^{-1}, that of water. Nearest neighbor searches were of grid type, using a group cutoff scheme with update frequency of 10 steps and a neighbor list cutoff of 0.9 nm. Nonbonded interactions were treated with a twin range cutoff scheme, with cutoff distances 1.4 nm for van der Waals energies and 0.9 nm for Coulombic energies. Long-range electrostatics were evaluated using a fourth-order particle mesh Ewald sum of spacing 0.12 nm^{-1} with relative tolerance 1×10^{-5}. All bonds were constrained with the LINCS algorithm, and cubic periodic boxes of size (L_x, L_y, L_z) = (5.5, 5.5, 5.5) nm were used as the simulation cell (17–20).

In addition to the REMD simulations, we also performed long simulations with explicit chromophores attached to the peptides. These simulations utilized the Amber ff99SBws force field for the protein, and the Amber-Dyes force field (21) for the chromophores. One minor and likely inconsequential correction was made to the force field: the maleimide-thiol conjugates in the original force field had an incorrect structure (the carbon-carbon double bond was retained in the product). A corrected version of the force field and scripts to add the chromophores to an existing protein structure are available from http://www.github.com/bestlab.

In all analyses shown, frames in which the peptides were within 4.5 Å of their periodic image were discarded to remove unphysical configurations. We discarded the first 375 ns of the trajectories as conformational equilibration (see Fig. S10 *E* and *F*), and time-series of the relevant measurements were generated every 50 ps.

Geometric and *E* analysis. Time-series of the radius of gyration R_g and end-to-end distance R_{ee} were calculated using respectively the `g_gyrate` and `g_dist` utilities of Gromacs. We took R_{ee} as the distance between Cα atoms of the N- and C-termini. Time-series of the FRET efficiency were generated by conversion of the R_{ee} time-series according to the following equation:

$$E(t) = \frac{1}{1 + \left(R'_{ee}(t) / R_0\right)^6}, \tag{S18}$$

where we accounted for the effects of the experimental dyes by treating them as 12 extra amino acid residues and assuming a Gaussian scaling exponent (22):

$$R'_{ee}(t) = R_{ee}(t)\left(\frac{N+12}{N}\right)^{0.5}, \tag{S19}$$

where N is either 40 or 42, depending on the peptide isoform.

Time-series of the hydrodynamic radius R_H were generated using the program Hydropro (23) every 50 ps. Specifically, a shell-method calculation was run with the radius of primary elements equal to a = 0.29 nm, with three minibead iterations running from minibead radii σ = 0.1 to 0.2 nm. The temperature was taken to be 25.85°C, the solvent viscosity 0.01 Poise, the solvent density 1.0 gcm^{-3}, the partial specific volume of the peptide 0.741 $\mathrm{cm}^3\mathrm{g}^{-1}$ and a molecular weight of the peptide equal to 4329.9 Da (Aβ40) or 4514.1 Da (Aβ42). The resultant translational diffusion constants were then transformed to hydrodynamic radii using the Stokes-Einstein equation with a temperature of 299 K and a solvent viscosity of 0.01 Poise.

Averages of all quantities were calculated and errors generated using block averaging with 10 blocks, with the results for R_g, R_{ee}, and E shown in Figs. 6 and S2 for respectively the Amber ff99SBws and Amber ff03ws force fields. For the hydrodynamic radius, these block errors were combined in quadrature with an assumed systematic error of 5% in estimating the diffusion constant (23).

Contact and cluster analysis. Time-dependent inter-residue distance matrices were calculated from non-hydrogen atoms using `g_mdmat` every 50 ps, and converted to contact probability maps $C(t)$ using the continuous transformation:

$$C_{ij}(t) = \frac{1}{1 + \exp\left[\beta\left(r_{ij}(t) - r_0\right)\right]}, \tag{S20}$$

with $\beta = 500\ \mathrm{nm}^{-1}$ and $r_0 = 4.5$ Å.

Time-averaged contact probability maps $\langle C \rangle_t$ for all simulations were generated by directly counting the fraction of frames in which residues i and j were within 4.5 Å of each other.

To extract the conformational ensemble, we performed a clustering analysis using the k-means algorithm as implemented in the `scipy.cluster.vq` module, with our raw data being the intramolecular contact maps $C(t)$ ignoring all (i, i), $(i, i+1)$, $(i, i+2)$, $(i, i+3)$ and $(i, i+4)$ contacts in order to extract long-range contact information about the peptide ensembles. Note that the number of clusters allowed by the data is constrained above by $k_{\text{max}} = \left\lfloor \frac{2N_{\text{frames}}}{N_{\text{res}}^2 - 9N_{\text{res}} + 20} \right\rfloor$, where N_{frames} is the number of acceptable (i.e., without periodic contact) frames analyzed, and N_{res} is the length of the peptide primary sequence (i.e., either 40 or 42). This limit comes because in any data fitting problem, the number of fit parameters cannot exceed the number of data points. In these analyses, the number of fit parameters is the number of unique intra-residue contact probabilities (excluding up to and including i to i+4 contacts) multiplied by the number of clusters k: $N_{\text{fit}} = k[N_{\text{res}}(N_{\text{res}} + 1)/2 - 5N_{\text{res}} + 10]$. The number of data points is the number of frames analyzed, as each frame is one possible intra-peptide correlation: $N_{\text{data}} = N_{\text{frames}}$. Equating the two $N_{\text{fit}} = N_{\text{data}}$ so as just to avoid overfitting gives the constraint. Inserting the relevant values gives k_{max} = 11 (10) and 11 (11) respectively for Aβ40 (Aβ42) using the Amber ff99SBws and Amber ff03ws force fields. At this upper limit, however, each fit parameter is only constrained by one data point; to avoid such overfitting we tried clustering for values of k until only $k = 7$, when each fit parameter is constrained by approximately 1.5 data points.

We determined that three clusters were enough to describe the average data in all cases except for the Aβ42 Amber ff03ws trajectory, which needed four clusters. The manner in which we decided the appropriate number of clusters was to construct the metric $\Delta = ||\langle C\rangle_t, \langle C\rangle_k||$, which measures the L_2 distance between the contact map constructed by averaging the contact maps at every time $\langle C\rangle_t$ and the contact map constructing by taking an average of the contact maps of the frames closest to the cluster centers (in contact map space) determined by the algorithm, weighed by the population of each cluster, or $\langle C\rangle_k$. As shown in Fig. S5, this metric is generally decreasing with increasing k, but to avoid over-fitting the data we imposed a cutoff in the fractional decrease in Δ of 10%, which we believe balances the need to describe sufficiently the ensemble against the risk of over-fitting. The contact maps shown in Figs. 7 and S9 are the average contact maps of all frames assigned to each cluster, and the structures shown are those frames that were closest to the determined cluster centers.

To test for the robustness of our clustering analysis, as the k-means algorithm is ultimately stochastic, we repeated the same clustering procedure a second time for both Aβ isoforms, for each of the Amber ff99SBws and ff03ws force fields, with the results summarized in Table S4. In this table, $p_k(\in 2 \mid \in 1)$ is the conditional probabilities that if a frame were assigned to cluster k the first time, it would be assigned to the same cluster the second, and $p_k(\in 1 \mid \in 2)$ the reverse probability. The last column $||C_1, C_2||_k$ is the L_2 distance between the average contact maps of the kth cluster generated from the first and second times. As can be seen, there is an extremely high degree of reproducibility in frame assignments, as demonstrated by the near-unity values of the conditional probabilities and the small distances between average contact maps for the same cluster, implying that our clustering was robust. For a sense of scale, the (unitless) distance between the average contact maps of the two major clusters for Aβ40 in the ff99SBws force field is 1.726, and the distance between the most-populated and least-populated clusters is 6.046.

The residue-specific average β-sheet likelihood for each cluster was calculated using the DSSP algorithm (24) as implemented in the `do_dssp` algorithm of Gromacs as the fraction of frames in which each residue was assigned to be in the β-sheet conformation, and the excess β-sheet likelihood of each residue in each cluster was defined as the difference between this β-sheet likelihood and the ensemble-averaged β-sheet likelihood per residue. Results are shown in Fig. S6 *A*.

NMR analysis. Dihedral angle ($\phi_i(t)$, $\psi_i(t)$) trajectories for each non-terminal residue at 277 K were generated using `g_rama`, and these were converted to residue-specific ${}^3J_{\mathrm{HNH}\alpha}(i)$ coupling constants using the Karplus equation:

$$ {}^3J_{\mathrm{HNH}\alpha}(i,t) = A\cos^2(\phi_i(t) - 60°) + B\cos(\phi_i(t) - 60°) + C\,, \tag{S21}$$

with *A*, *B* and *C* parameters taken from (25) as $A = 7.97$ Hz, $B = -1.26$ Hz and $C = 0.63$ Hz. The coupling constants were then time-averaged and errors were taken as a combination in quadrature of simulation errors by block averaging with 10 blocks and modelling errors due to uncertainties in the determination of the Karplus parameters:

$$(\Delta^3 J_{\mathrm{HNH}\alpha}(i))^2 = (\Delta_{\mathrm{block}})^2 + (\Delta_{\mathrm{Karplus}})^2\,, \tag{S22}$$

where we estimated the Karplus error term $\Delta_{\mathrm{Karplus}} = 0.42$ Hz, the RMSD of fitting experimental data in (25).

These coupling constants were then compared against experimentally determined coupling constants as published in (26) to validate our force fields, with the results shown in Figs. 6 and S9. For comparison we use the reduced χ^2, defined as

$$\chi^2 = \frac{1}{N}\sum_{i=1}^{N}\frac{\left(J_{\mathrm{expt}}(i) - J_{\mathrm{sim}}(i)\right)^2}{\left(\Delta J(i)\right)^2}\,, \tag{S23}$$

in which $J_{\mathrm{expt}}(i)$, $J_{\mathrm{sim}}(i)$ and $\Delta J(i)$ are respectively the experimental value, simulation value and estimated error (Eq. S22) for scalar coupling *i*.

Calculation of chemical shifts. Secondary chemical shift deviations with respect to the random coil are calculated as follows: $\Delta\delta\mathrm{C}\alpha = (\delta\mathrm{C}\alpha_{\mathrm{sim}} - \delta\mathrm{C}\alpha_{\mathrm{ref}})$ and $\Delta\delta\mathrm{C}' = (\delta\mathrm{C}'_{\mathrm{sim}} - \delta\mathrm{C}'_{\mathrm{ref}})$, where $\delta\mathrm{C}\alpha_{\mathrm{sim}}$ and $\delta\mathrm{C}'_{\mathrm{sim}}$ are predicted Cα and C′ chemical shifts from simulation ensembles using an empirical chemical shift deviation prediction algorithm, SPARTA+ (27). $\delta\mathrm{C}\alpha_{\mathrm{ref}}$ and $\delta\mathrm{C}'_{\mathrm{ref}}$ respectively are the calculated Cα and C′ random coil reference chemical shifts computed using the Poulsen IDP/IUP random coil chemical shifts calculator at 277 K and pH 7 (28, 29). Errors are predicted by standard block averaging using 10 equal non-overlapping blocks of the data. Results are shown in Fig. S4.

Internal peptide scalings. To obtain information on the relevant intramolecular interactions, we performed a scaling analysis of both isoforms using polymer theory. Namely, we calculated the average inter-Cα atom distance between all residue as a function of sequence separation $|i - j|$ using `g_traj`. Assuming Flory-like behavior, then, these distances should follow a power law:

$$\langle r_{|i-j|} \rangle = b|i-j|^{\nu}, \tag{S23}$$

where b is the effective length of uncorrelated segments and ν is the scaling exponent, which contains information on the interactions between monomers. The averaging brackets are taken over the inter-residue time-series and over all amino acids $|i - j|$ away from each other in the primary structure. Errors were calculated by block averaging using 10 blocks, and a linear fit of $\ln \langle r_{|i-j|} \rangle$ vs. $\ln |i - j|$, weighted by each point's relative block error, yielded ν, using the standard $b = 0.55$ nm (30). In practice, we fit distances only for $|i - j| \geq 10$, so as not to include the effects of short-range backbone rigidity.

The results are shown in Figs. 7 and S9 respectively for the Amber ff99SBws and Amber ff03ws force fields, and show that both Aβ40 and Aβ42 follow extremely similar short-range behavior, but diverge at long ranges, where the shorter peptide is more expanded than the longer, indicating that long-range attractive contacts account for the observed slight collapse of Aβ42, or that long-range repulsive interactions expand Aβ40. The values of the scaling exponents are around 0.5, as expected for IDP's at or near the Θ-point.

References

1. Young, T.S., I. Ahmad, J.A. Yin, and P.G. Schultz. 2010. An enhanced system for unnatural amino acid mutagenesis in E. coli. *J Mol Biol*. 395: 361–374.
2. Nettels, D., S. Müller-Späth, F. Küster, H. Hofmann, D. Haenni, S. Rüegger, L. Reymond, A. Hoffmann, J. Kubelka, B. Heinz, K. Gast, R.B. Best, and B. Schuler. 2009. Single-molecule spectroscopy of the temperature-induced collapse of unfolded proteins. *Proc Natl Acad Sci U S A*. 106: 20740–20745.
3. Chung, H.S., J.M. Louis, and W.A. Eaton. 2009. Experimental determination of upper bound for transition path times in protein folding from single-molecule photon-by-photon trajectories. *Proc Natl Acad Sci U S A*. 106: 11837–11844.
4. Zheng, Q., S. Jockusch, Z. Zhou, and S.C. Blanchard. 2014. The contribution of reactive oxygen species to the photobleaching of organic fluorophores. *Photochem Photobiol*. 90: 448–454.
5. Zheng, Q., M.F. Juette, S. Jockusch, M.R. Wasserman, Z. Zhou, R.B. Altman, and S.C. Blanchard. 2014. Ultra-stable organic fluorophores for single-molecule research. *Chem Soc Rev*. 43: 1044–1056.
6. Chung, H.S., F. Meng, J.-Y. Kim, K. McHale, I. V. Gopich, and J.M. Louis. 2017. Oligomerization of the tetramerization domain of p53 probed by two- and three-color single-molecule FRET. *Proc Natl Acad Sci U S A*. 114: E6812–E6821.
7. Merchant, K.A., R.B. Best, J.M. Louis, I. V Gopich, and W.A. Eaton. 2007. Characterizing the unfolded states of proteins using single-molecule FRET spectroscopy and molecular simulations. *Proc Natl Acad Sci U S A*. 104: 1528–1533.
8. Gopich, I. V., and A. Szabo. 2012. Theory of single-molecule FRET efficiency histograms. *Adv Chem Phys*. 146: 245–297.
9. Chung, H.S., J.M. Louis, and I. V. Gopich. 2016. Analysis of fluorescence lifetime and energy transfer efficiency in single-molecule photon trajectories of fast-folding proteins. *J Phys Chem B*. 120: 680–699.
10. Gopich, I. V, and A. Szabo. 2009. Decoding the pattern of photon colors in single-molecule FRET. *J Phys Chem B*. 113: 10965–10973.
11. Soranno, A., B. Buchli, D. Nettels, R.R. Cheng, S. Müller-Späth, S.H. Pfeil, A. Hoffmann, E.A. Lipman, D.E. Makarov, and B. Schuler. 2012. Quantifying internal friction in unfolded and intrinsically disordered proteins with single-molecule spectroscopy. *Proc Natl Acad Sci U S A*. 109: 17800–17806.
12. Nettels, D., I. V Gopich, A. Hoffmann, and B. Schuler. 2007. Ultrafast dynamics of protein collapse from single-molecule photon statistics. *Proc Natl Acad Sci U S A*. 104: 2655–2660.
13. Gopich, I. V, D. Nettels, B. Schuler, and A. Szabo. 2009. Protein dynamics from single-molecule fluorescence intensity correlation functions. *J Chem Phys*. 131: 95102.
14. Best, R.B., W. Zheng, and J. Mittal. 2014. Balanced protein–water interactions improve properties of disordered proteins and non-specific protein association. *J Chem Theory*

Comput. 10: 5113–5124.

15. Páll, S., M.J. Abraham, C. Kutzner, B. Hess, and E. Lindahl. 2015. Tackling Exascale Software Challenges in Molecular Dynamics Simulations with GROMACS. In: Lecture Notes in Computer Science (including subseries Lecture Notes in Artificial Intelligence and Lecture Notes in Bioinformatics). . pp. 3–27.
16. Abascal, J.L.F., and C. Vega. 2005. A general purpose model for the condensed phases of water: TIP4P/2005. *J Chem Phys*. 123: 234505.
17. Parrinello, M., and A. Rahman. 1981. Polymorphic transitions in single crystals: A new molecular dynamics method. *J Appl Phys*. 52: 7182–7190.
18. Nosé, S., and M.L. Klein. 1983. Constant pressure molecular dynamics for molecular systems. *Mol Phys*. 50: 1055–1076.
19. Essmann, U., L. Perera, M.L. Berkowitz, T. Darden, H. Lee, and L.G. Pedersen. 1995. A smooth particle mesh Ewald method. *J Chem Phys*. 103: 8577–8593.
20. Hess, B., H. Bekker, H.J.C. Berendsen, and J.G.E.M. Fraaije. 1997. LINCS: A linear constraint solver for molecular simulations. *J Comput Chem*. 18: 1463–1472.
21. Graen, T., M. Hoefling, and H. Grubmüller. 2014. AMBER-DYES: Characterization of Charge Fluctuations and Force Field Parameterization of Fluorescent Dyes for Molecular Dynamics Simulations. *J Chem Theory Comput*. 10: 5505–5512.
22. Zheng, W., A. Borgia, K. Buholzer, A. Grishaev, B. Schuler, and R.B. Best. 2016. Probing the action of chemical denaturant on an intrinsically disordered protein by simulation and experiment. *J Am Chem Soc*. 138: 11702–11713.
23. Ortega, A., D. Amorós, and J. García De La Torre. 2011. Prediction of hydrodynamic and other solution properties of rigid proteins from atomic- and residue-level models. *Biophys J*. 101: 892–898.
24. Kabsch, W., and C. Sander. 1983. Dictionary of protein secondary structure: Pattern recognition of hydrogen bonded and geometrical features. *Biopolymers*. 22: 2577–2637.
25. Vögeli, B., J. Ying, A. Grishaev, and A. Bax. 2007. Limits on variations in protein backbone dynamics from precise measurements of scalar couplings. *J Am Chem Soc*. 129: 9377–9385.
26. Roche, J., Y. Shen, J.H. Lee, J. Ying, and A. Bax. 2016. Monomeric Aβ1–40 and Aβ1–42 peptides in solution adopt very similar Ramachandran map distributions that closely resemble random coil. *Biochemistry*. 55: 762–775.
27. Shen, Y., and A. Bax. 2010. SPARTA+: A modest improvement in empirical NMR chemical shift prediction by means of an artificial neural network. *J Biomol NMR*. 48: 13–22.
28. Kjaergaard, M., S. Brander, and F.M. Poulsen. 2011. Random coil chemical shift for intrinsically disordered proteins: Effects of temperature and pH. *J Biomol NMR*. 49: 139–149.
29. Kjaergaard, M., and F.M. Poulsen. 2011. Sequence correction of random coil chemical shifts: Correlation between neighbor correction factors and changes in the Ramachandran distribution. *J Biomol NMR*. 50: 157–165.

30. Hofmann, H., A. Soranno, A. Borgia, K. Gast, D. Nettels, and B. Schuler. 2012. Polymer scaling laws of unfolded and intrinsically disordered proteins quantified with single-molecule spectroscopy. *Proc Natl Acad Sci U S A*. 109: 16155–16160.

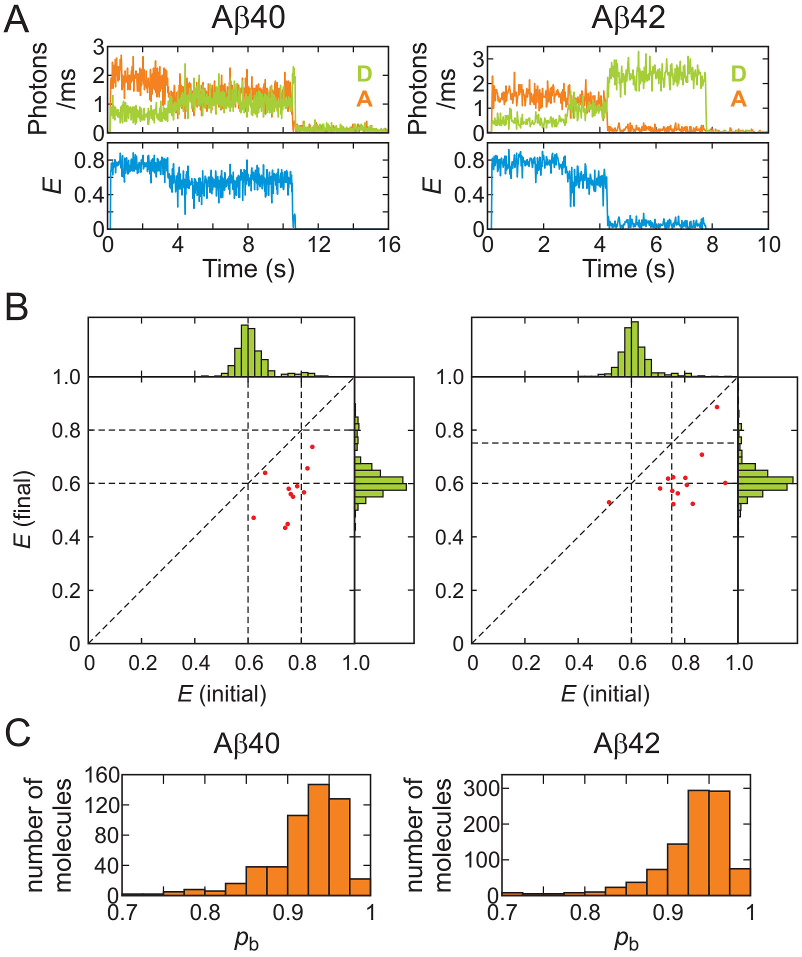

Figure S1. Alexa 647 photophysics. (*A*) Trajectories exhibiting FRET efficiency changes from *E* ~ 0.8 to *E* ~ 0.6. (*B*) Transition maps show that the transitions are localized on the lower right side of the diagonal, indicating that these transitions are irreversible on the time scale of tens of seconds. Similar irreversible transitions have been observed and attributed to the changes in the extinction coefficient of Alexa 647 (6). (*C*) The distribution of the acceptor bright state population extracted from the data in Fig. 4 using the maximum likelihood method with the 1-state acceptor blinking model.

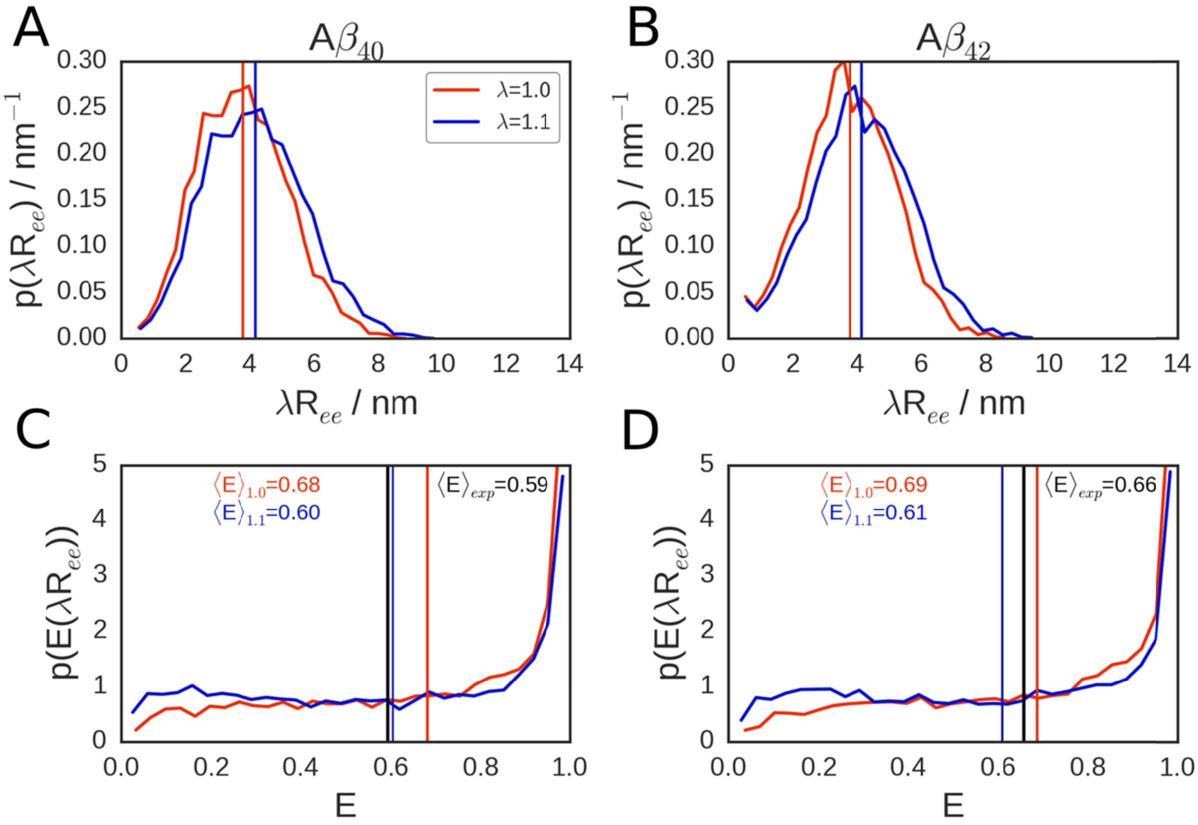

Figure S2. Sensitivity of FRET parameters to end-to-end distance distributions. For both Aβ40 (left) and Aβ42 (right), (*A*, *B*) scaling length scale for the end-to-end distance probability densities obtained from simulation (red) by a factor of 1.1 (blue) results in (*C*, *D*) FRET efficiency distributions whose means (colored vertical lines) are similar to or slightly smaller than the experimentally determined values (black vertical lines) for the freely diffusing peptides. Thus a shift of the distances of less than 10% would be sufficient to match the experimental distribution.

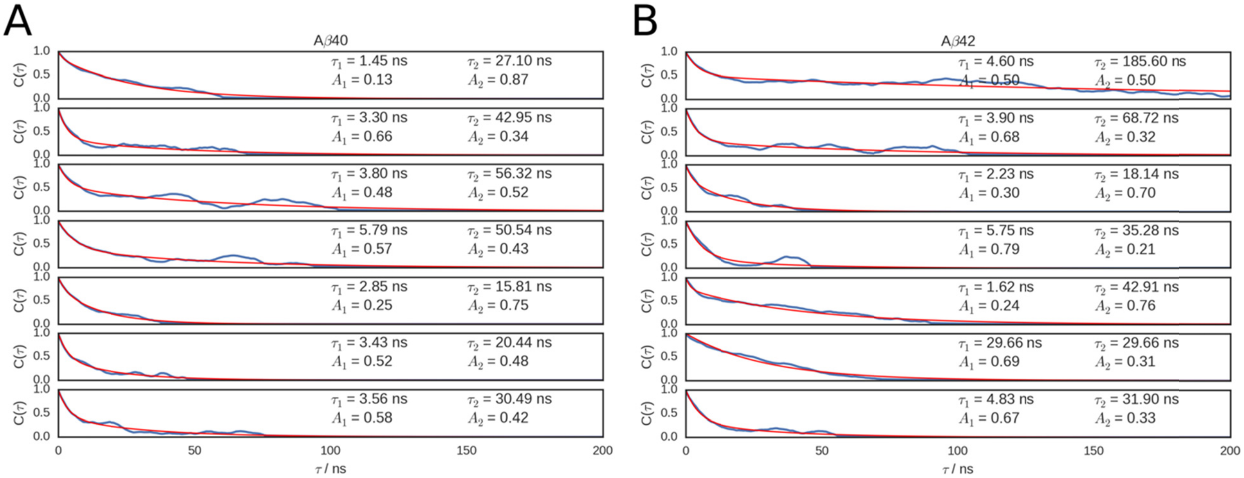

Figure S3. FRET efficiency autocorrelation functions *C*(τ) for simulations of dye-labelled Aβ40 (*A*) and Aβ42 (*B*), for each of the seven replicates, excluding the first 200 ns of data as equilibration. Blue curves are data and red are biexponential fits, with insets showing the fit results for decay times (τ_i) and exponential amplitudes (A_i). Averaging gives decay times of $\langle\tau_1\rangle$ = 3.5 ± 0.5 ns (8 ± 3 ns) and $\langle\tau_2\rangle$ = 35 ± 5 ns (60 ± 20 ns) for Aβ40 (Aβ42). The slow decay time is in quantitative agreement with the reconfiguration time determined from FRET experiments.

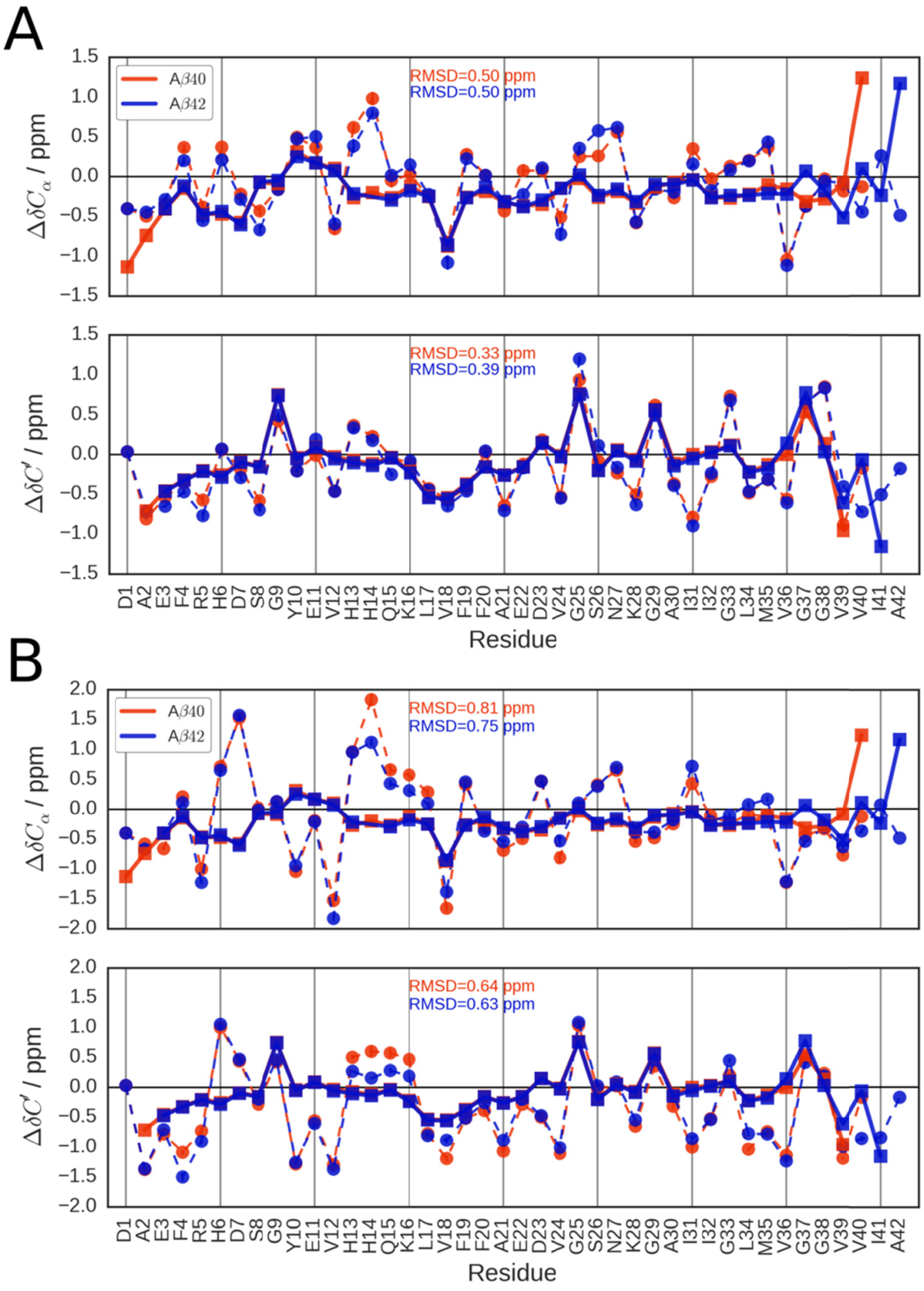

Figure S4. Comparison of secondary carbon chemical shifts between simulation (277 K) and experiment (26) with (*A*) Amber ff99SBws and (*B*) Amber ff03ws force fields. Simulation results are in circles and dashed lines while experimental results are in squares and thick solid lines. The shifts are relative to predicted random coil values. The root-mean-squared deviation, RMSD, between predicted values from simulations and experimental values are overlain, with results showing an agreement closer than the precision of shift prediction algorithm (see the text).

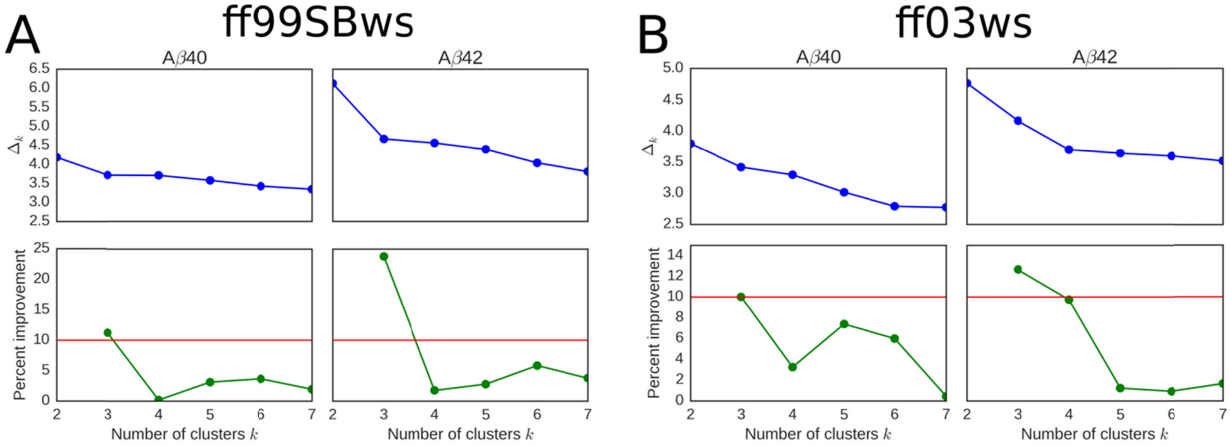

Figure S5. Determination of the number of clusters needed to describe the structural ensemble of (left column) Aβ40 and (right column) Aβ42 using the (*A*) Amber ff99SBws and (*B*) Amber ff03ws force field. Percent improvement in adding the k^{th} cluster is defined as $100 \times |\Delta_k - \Delta_{k-1}| / \Delta_2$, which measures the fractional improvement in capturing the ensemble-averaged contact map when an extra cluster center is added, relative to using only two clusters. In all cases, using more than three clusters results in insignificant (< 10%) improvement in describing the ensemble and comes at the cost of overfitting the data, save for the Aβ42 in Amber ff03ws, which requires four clusters.

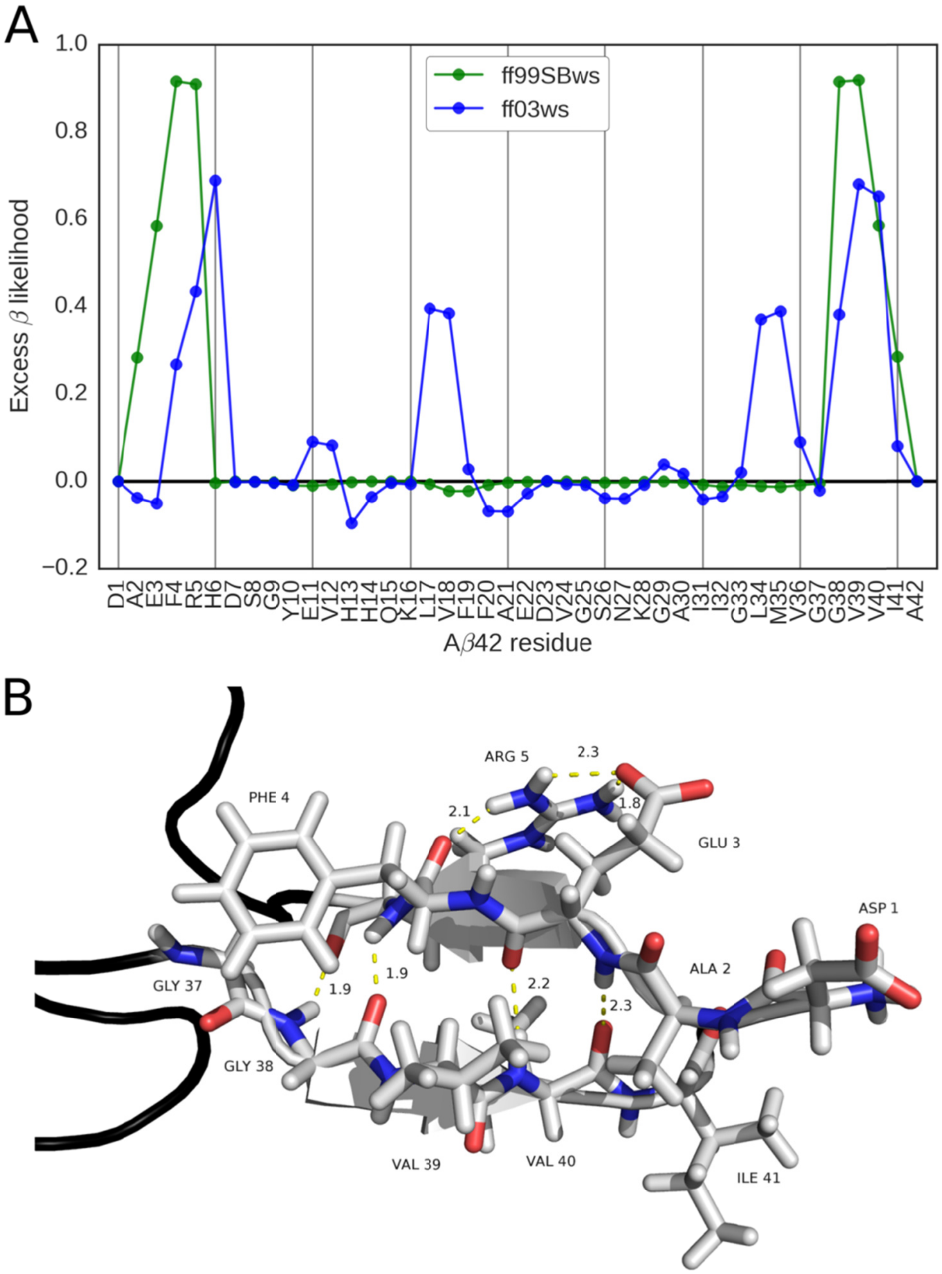

Figure S6. (*A*) Excess β-sheet likelihood, as defined in the SI section "Contact and cluster analysis", of the minor hairpin cluster of Aβ42 using the Amber ff99SBws and Amber ff03ws force fields. Both show significantly elevated propensity at the termini, demonstrating that these structures are true hairpins. (*B*) Terminal contacts of the Aβ42 hairpin conformation shown in Fig. 7(*D*). The hairpin is stabilized by hydrogen bonding between the backbone atoms of N-terminal residues 1 - 5 and C-terminal residues 38 - 41. Note that a similar structure for Aβ40 would be disfavored as the carboxyl group of the C-terminal V40 would be charged at physiological pH. The structure was made using PyMOL (Schrödinger, LLC), and the distances of the highlighted hydrogen bonds are in units of Angstroms.

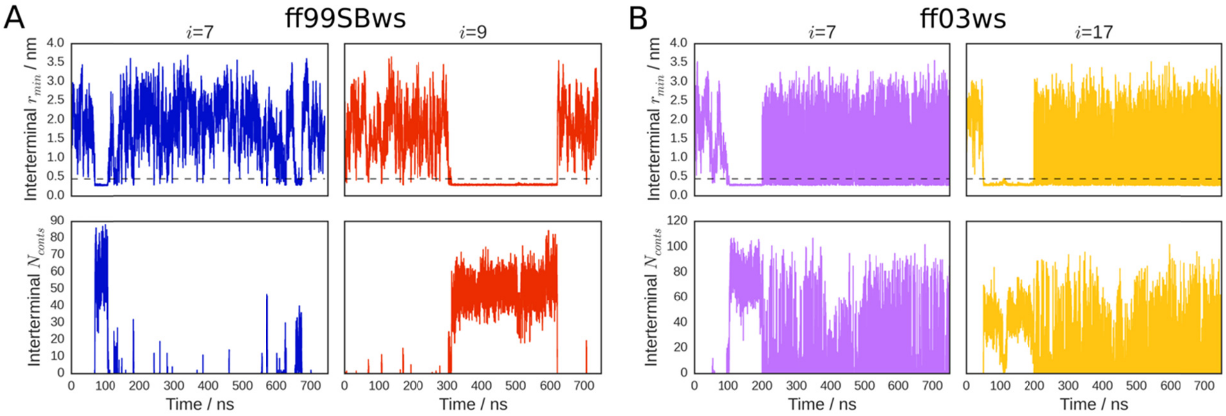

Figure S7. Reversibility of inter-terminal contacts. Minimum distance (top) and number of contacts (bottom) trajectories for the inter-terminal groups of Aβ42 in the Amber ff99SBws (*A*) and ff03ws (*B*) force fields, obtained from continuous REMD trajectories (i.e. followed through swaps in temperature space). Data are shown for only the two replicas with the highest contact population in each case, although other trajectories also showed contacts. As the observed contact maps of the minor hairpin clusters showed a small difference in contacting residues for each force field (see Figures 7(*D*) and S3(*D*)), we employed the following definitions of N- and C-termini: residues 2-5 and 38-41 for ff99SBws and residues 3-6 and 38-41 for 03ws.

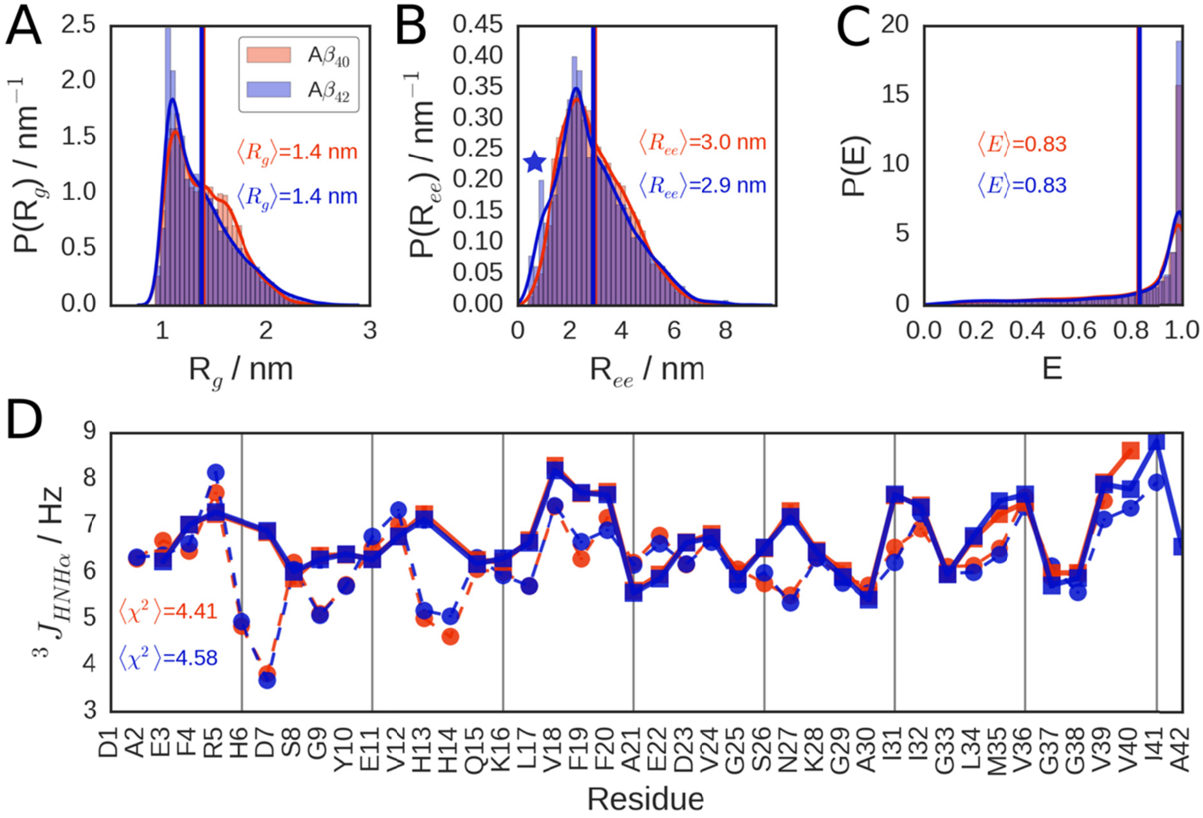

Figure S8. Ensemble observables for Aβ40 and Aβ42 using the Amber ff03ws force field. The results are consistent with the Amber ff99SBws results shown in Fig. 6.

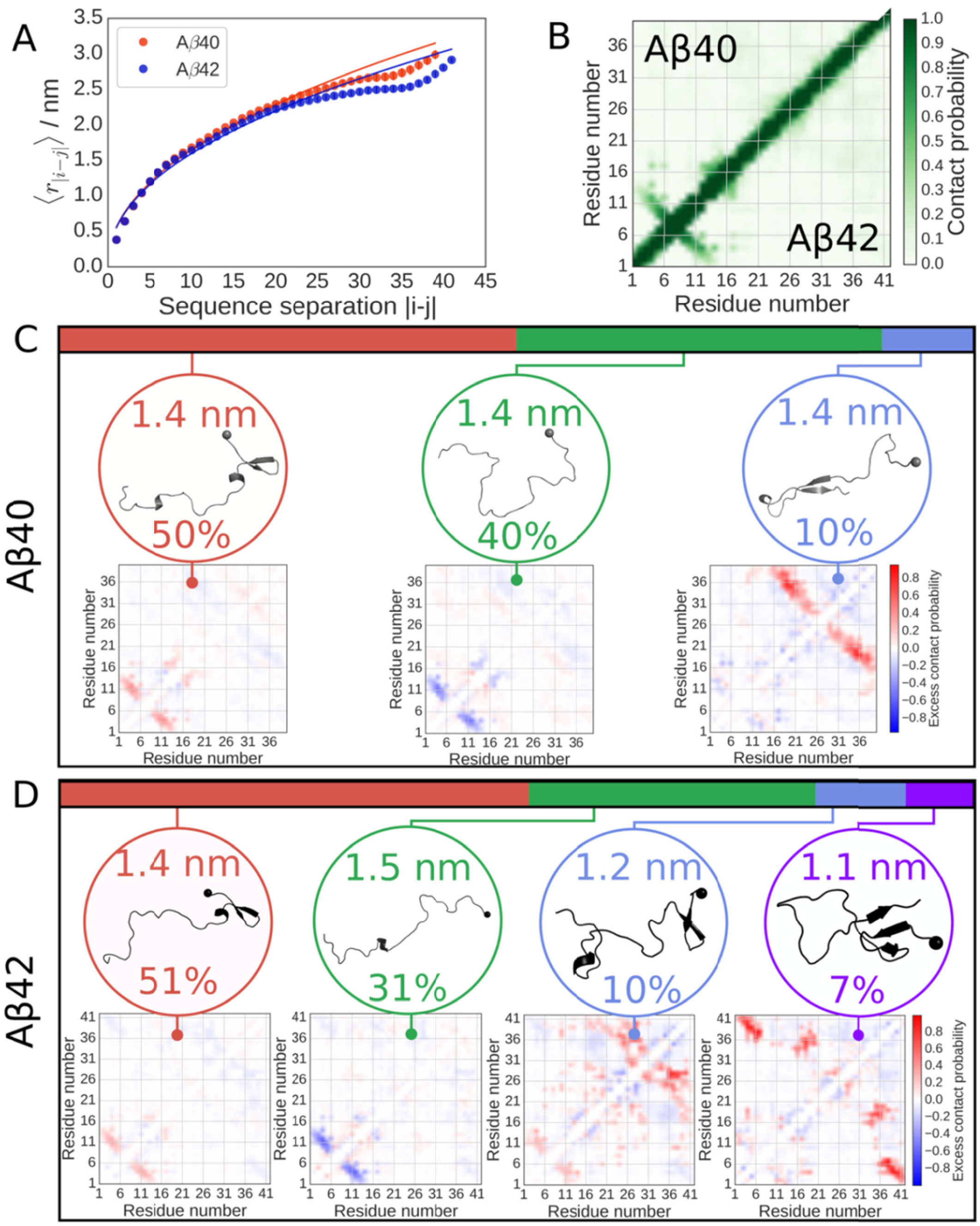

Figure S9. Conformational ensembles of Aβ40 and Aβ42 using the Amber ff03ws force field showing (*A*) internal Cα atom distance scalings for each peptide, with data shown as circles, and fits to a power law as described in the SI as solid lines, giving scaling exponents of ν = 0.4764 ± 0.0007 and 0.4625 ± 0.0006 respectively for Aβ40 and Aβ42. Also shown are the ensemble-averaged intramolecular contact maps (*B*) and cluster-averaged contact maps and most representative structures for Aβ40 (*C*) and Aβ42 (*D*). The results are consistent with the amber ff99SBws results shown in Fig. 7, save for significant population of hairpin structure in the N-terminal region for both peptides. Importantly, a hairpin formed by terminal contacts appears in the smallest cluster of the Aβ42 ensemble, as observed with Amber ff99SBws.

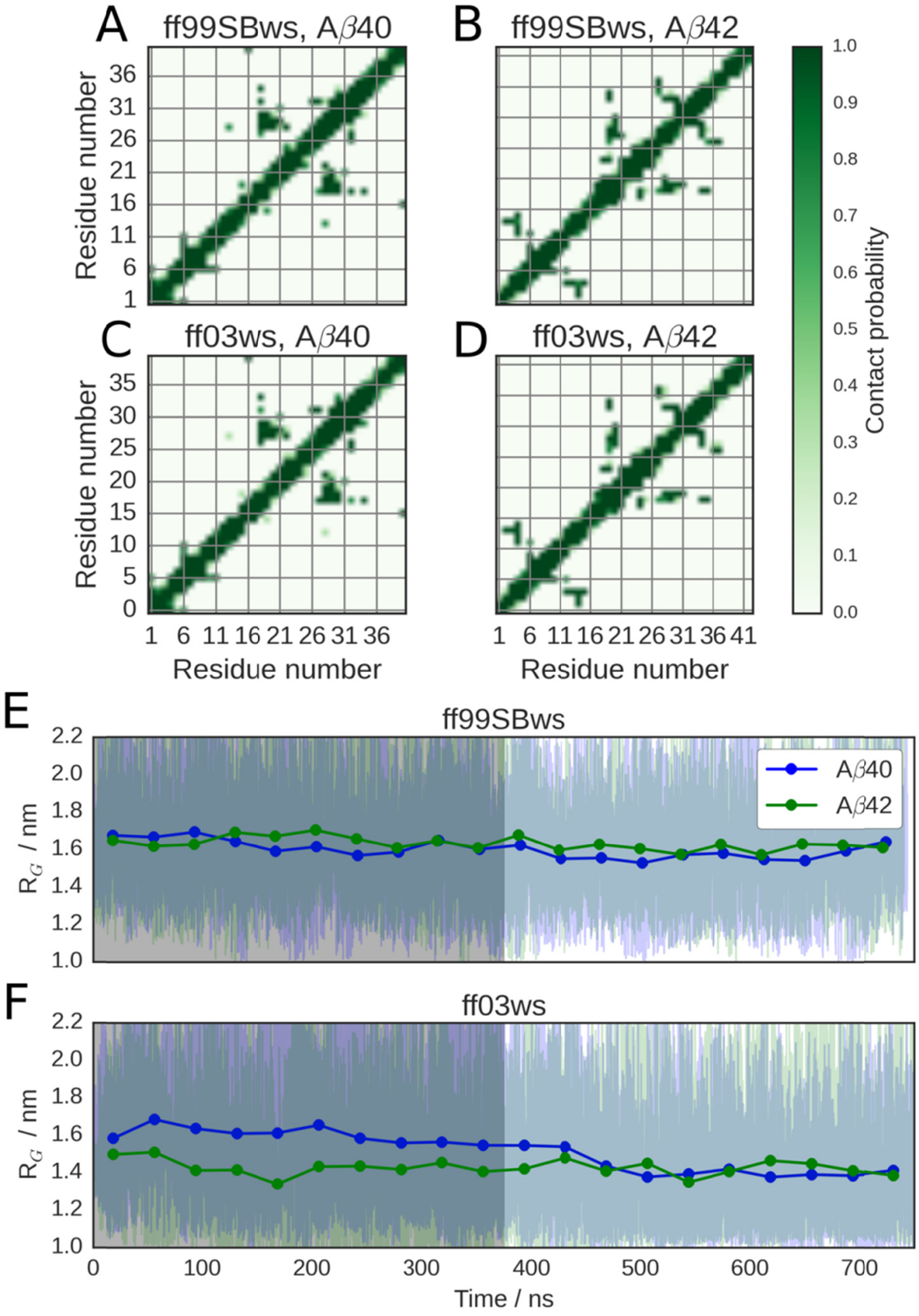

Figure S10. Initial configurations for Amber ff99SBws (*A, B*) and Amber ff03ws (*C, D*) force field REMD simulations, for both Aβ40 (*A, C*) and Aβ42 *(B, D)* peptides. Time-series of the radius of gyration R_g for both peptide isoforms using Amber ff99SBws (*E*) and Amber ff03ws (*F*) force fields. Light lines are raw data, thick circles and lines are block averages by dividing the simulation into 20 equal blocks and the light gray area is the first half of each simulation discarded as NPT equilibration when there is still a systematic drift in at least one of the peptide/force field combinations. Data taken from the 299 K replica.

Table S1. Comparison of the FRET efficiencies of Aβ40 and Aβ42 measured in PBS, and computed from simulation.

Experiment/Simulation	Construct	Aβ40	Aβ42
Free Diffusion[a]	Aβ	0.592 (± 0.005)	0.658 (± 0.002)
	Avi-Aβ	0.560 (± 0.005)	0.583 (± 0.004)
Immobilization (CW excitation)[b]	Avi-Aβ	0.572 (± 0.001)	0.581 (± 0.001)
Immobilization (Pulsed excitation)[c]	Avi-Aβ	0.600 (± 0.002)	0.604 (± 0.002)
Amber ff99SBws (implicit dyes)	Aβ	0.68 (± 0.01)	0.69 (± 0.01)
Amber ff99SBws (explicit dyes)	Aβ	0.75 (± 0.02)	0.79 (± 0.02)
Amber ff03ws (implicit dyes)	Aβ	0.83 (± 0.01)	0.833 (± 0.006)

[a] Errors are standard deviations obtained from the fitting of the FRET efficiency histograms in Fig. 2 to the Gaussian function. FRET efficiencies were corrected for background, donor leak, and γ-factor.

[b] Errors are standard deviations obtained from the diagonal elements of the covariance matrix calculated from the likelihood function (1-state with acceptor blinking) in Table S2. FRET efficiencies were corrected for background, donor leak, γ-factor, direct acceptor excitation, and acceptor blinking.

[c] Errors are standard deviations obtained from the fitting of the FRET efficiency histograms in Fig. 4B to the Gaussian function. FRET efficiencies were corrected for background, donor leak, γ-factor, direct acceptor excitation, and acceptor blinking.

Table S2. Maximum likelihood analysis parameters.[a]

Model	Parameters	Aβ40	Aβ42
2-state	E_1	0.598 (± 0.001)	0.614 (± 0.001)
	E_2	0.133 (± 0.004)	0.134 (± 0.004)
	k / ms^{-1}	12.2 (± 0.3)	14.1 (± 0.4)
	p_1	0.935 (± 0.002)	0.937 (± 0.002)
1-state with acceptor blinking	E	0.592 (± 0.001)	0.608 (± 0.001)
	k_b / ms^{-1}	11.7 (± 0.3)	13.1 (± 0.4)
	p_b	0.942 (± 0.001)	0.949 (± 0.001)
Donor-acceptor cross-correlation	k / ms^{-1}	15.3 (± 2.9)	16.5 (± 4.5)

[a] Errors are standard deviations obtained from the diagonal elements of the covariance matrix calculated from the likelihood function. The extracted FRET efficiencies are uncorrected values (apparent FRET efficiencies).

Table S3. Effect of excluding frames in which dyes (explicit dye simulations) or termini (implicit dye simulations) are in contact, for several definitions of contact cutoff. Contacts are defined as the minimum distance between any pair of heavy atoms, one from each contacting group.

	Amber ff99SBws, explicit dyes			
	No exclusions	Exclude ≤ 0.45 nm	Exclude ≤ 0.75 nm	Exclude ≤ 1.0 nm
$\langle E \rangle_{\mathrm{A\beta40}}$	0.75 ± 0.02	0.75 ± 0.02	0.75 ± 0.02	0.74 ± 0.02
$\langle E \rangle_{\mathrm{A\beta42}}$	0.79 ± 0.02	0.78 ± 0.02	0.77 ± 0.02	0.77 ± 0.02
	Amber ff99SBws, implicit dyes			
	No exclusions	Exclude ≤ 0.45 nm	Exclude ≤ 0.75 nm	Exclude ≤ 1.0 nm
$\langle E \rangle_{\mathrm{A\beta40}}$	0.68 ± 0.01	0.68 ± 0.01	0.68 ± 0.01	0.68 ± 0.01
$\langle E \rangle_{\mathrm{A\beta42}}$	0.69 ± 0.01	0.69 ± 0.01	0.682 ± 0.009	0.680 ± 0.009

Table S4. Reproducibility of *k*-means clustering, as measured by cluster-specific conditional probabilities of frame assignment overlap $p_k(\in 2 \mid \in 1)$ and $p_k(\in 1 \mid \in 2)$, as well as by average contact map distance $\|C_1, C_2\|_k$ between clusters.

Amber ff99SBws						
	Aβ40			Aβ42		
k	$p_k(\in 2 \mid \in 1)$	$p_k(\in 1 \mid \in 2)$	$\|C_1, C_2\|_k$	$p_k(\in 2 \mid \in 1)$	$p_k(\in 1 \mid \in 2)$	$\|C_1, C_2\|_k$
1	1.000	0.978	0.102	0.999	0.998	0.010
2	0.942	1.000	0.270	0.994	0.996	0.027
3	1.000	1.000	0.000	1.000	1.000	0.000
Amber ff03ws						
	Aβ40			Aβ42		
k	$p_k(\in 2 \mid \in 1)$	$p_k(\in 1 \mid \in 2)$	$\|C_1, C_2\|_k$	$p_k(\in 2 \mid \in 1)$	$p_k(\in 1 \mid \in 2)$	$\|C_1, C_2\|_k$
1	1.000	0.999	0.004	1.000	0.996	0.035
2	0.999	1.000	0.006	0.993	1.000	0.059
3	1.000	1.000	0.000	1.000	1.000	0.000
4	–	–	–	1.000	1.000	0.000